Comparing high-latitude thermospheric winds from FPI and CHAMP accelerometer measurements

Anasuya Aruliah[1,] Matthias Förster[2,3], Rosie Hood[1], Ian McWhirter[1], Eelco Doornbos[4,5]

[1]Atmospheric Physics Laboratory, University College London, Gower Street, London, WC1E 6BT, UK

[2]Helmholtz-Zentrum Potsdam, GFZ German Research Centre for Geosciences, Telegrafenberg, 14473 Potsdam, Germany

[3]Max Planck Institute for Solar System Research (MPS), Justus-von-Liebig-Weg 3, 37077 Göttingen, Germany

[4]Old affiliation: Faculty of Aerospace Engineering, Delft University of Technology (TU Delft), Kluyverweg 1, 2629 HS Delft, The Netherlands

[5]Current affiliation: Royal Netherlands Meteorological Institute (KNMI), Utrechtseweg 297, 3731 GA De Bilt, The Netherlands

Correspondence to: Anasuya Aruliah (a.aruliah@ucl.ac.uk), Matthias Förster (mfo@gfz-potsdam.de) and Eelco Doornbos (eelco.doornbos@knmi.nl)

Abstract. It is generally assumed that horizontal wind velocities are independent of height above the F_1-region (> 300 km) due to the large molecular viscosity of the upper thermosphere. This assumption is used to compare two completely different methods of thermospheric neutral wind observation, using two distinct locations in the high-latitude Northern Hemisphere. The measurements are from ground-based Fabry-Perot Interferometers (FPI), and from in-situ accelerometer measurements onboard the CHAMP satellite, which was in a near polar orbit. The UCL KEOPS FPI is located in the vicinity of the auroral oval at the ESRANGE site near Kiruna, Sweden (67.8°N, 20.4°E). The UCL Longyearbyen FPI is a polar cap site, located at the Kjell Henriksen Observatory on Svalbard (78.1°N, 16.0°E). The comparison is done in a statistical sense, comparing a longer time series obtained during nighttime hours in the winter months (DOY 300-65); with overflights of the CHAMP satellite between 2001 and 2007 over the observational sites, within ±2° latitude (±230 km horizontal range). The FPI is assumed to measure the line-of-sight winds at ~240 km height, i.e. the peak emission height of the atomic oxygen 630.0 nm emission. The cross-track winds are derived from state-of-the-art precision accelerometer measurements at altitudes between ~450 km (in 2001) to ~350 km (in 2007); i.e. 100-200 km above the FPI wind observations. We show that CHAMP winds at high latitudes are typically 1.5-2 times larger than FPI winds. In addition to testing the consistency of the different measurement approaches, the study aims to clarify the effects of viscosity on the height dependence of thermospheric winds.

1 Introduction

Global circulation models (GCM) of the upper atmosphere (80-600 km altitude) appear in two forms: climatologies based on empirical measurements, and theoretical models that calculate atmospheric conditions using the principles of physics and chemistry. These models are important for space weather studies and are also applied in understanding and predicting drag on low-altitude satellites, space debris, and the study of re-entry of near Earth objects. The theoretical and empirical models rely on observations from ground-based instruments

41 around the world and global observations by satellites to provide constraints and boundary conditions. In
42 particular, models must account for energy from sources external to the upper atmosphere (i.e., direct solar
43 radiation, particle precipitation and heat flow from above; radiative, conductive and convective heating from
44 below; the magnetospheric electrodynamic driver at high-latitudes), which is divided between acceleration of
45 the gas and heating. The empirical evidence for the energy budget can be provided by observations of winds and
46 temperatures.

48 The use of accelerometers on satellites to measure thermospheric winds had previously been reported quite
49 rarely (Marcos and Forbes, 1985; Forbes et al., 1993). Over the last few years CHAMP and GOCE winds have
50 been reported (e.g. Förster et al., 2008; Doornbos et al., 2010). The advantage of this technique consists in the
51 fairly direct in-situ measurement, with relatively high spatial (temporal) resolution, of the cross-track wind
52 component along the orbital track with only a limited number of special assumptions for the data interpretation.
53 Adding more satellites (e.g., GRACE and GRACE-FO), should allow better full wind vector reconstructions in
54 terms of statistical averages (Förster et al., 2008; Förster et al., 2017) as well as parameterized statistical studies
55 of the upper thermosphere dynamics in the near future. As a result, it makes it imperative that the derived winds
56 are correct because satellites provide global coverage of the upper atmosphere, unlike the small number of
57 ground-based instruments currently in existence. The larger databases and global coverage of the satellites will
58 particularly influence a semi-empirical model such as the Horizontal Wind Model (Drob et al., 2015), which is
59 commonly used as a climatology of winds to provide initial boundary conditions and validation for physics-
60 based global circulation models (GCMs).

62 In this paper we show that upper thermospheric winds measured by the CHAMP satellites are typically 1.5 to 2
63 times larger than those measured by ground-based Fabry-Perot Interferometers (FPIs) at an auroral site and
64 polar cap site. It is imperative to know whether this discrepancy is real (i.e. there is a variation of speed with
65 respect to height), or whether we have uncovered a problem of the absolute scaling of wind measurements by
66 comparing FPIs with CHAMP. With incorrect scaling, there arises a problem of distortion of energy budget
67 calculations of the upper atmosphere. A precise estimation of energy supply to the system is hindered
68 essentially, because the partitioning of kinetic and thermal energy channels becomes obscured. The acceleration
69 of the neutral air in 3-D space with respect to the active driver of the plasma motion is important to estimate, for
70 instance, the Joule heating rate as one of the most important thermal energy inputs. This has a knock-on effect
71 on the calculation of the absolute density of the gas, which is an important parameter used in, for example,
72 satellite orbit calculations.

74 **2 The CHAMP accelerometer data**

76 The challenging mini-satellite payload (CHAMP) was managed by the GFZ German Research Centre for
77 Geosciences of the Helmholtz Centre Potsdam. This mission was designed to perform detailed studies of the
78 Earth's gravitational and magnetic field with unprecedented accuracies and space/time resolutions as well as
79 GPS atmosphere and ionosphere profiling. The spacecraft was launched in July 2000 into a circular near-polar

80   orbit with 87.3° inclination at an initial altitude of ~460 km (Reigber et al., 2002). Its orbital altitude gradually

81   decayed to ~400 km in 2003 and ~330 km in 2008, and ended in September 2010.

82

83   One key scientific instrument onboard CHAMP was a triaxial accelerometer. It was located at the spacecraft's

84   center of mass and effectively probed the in-situ air drag. Thermospheric mass density and cross-track neutral

85   wind can be obtained from the drag acceleration observations. It is very difficult to determine the error estimate

86   because it depends on several variables as discussed in Doornbos et al. (2010) and shown in Table 5 from Visser

87   et al. (2019). This indicates that for force-derived winds, the largest sensitivity is to energy accommodation,

88   which is of the order of several tens of ms^{-1}.

89

90   A first analysis of the high-latitude thermospheric wind circulation in dependence on the IMF orientation was

91   performed by Förster et al. (2008) using the preliminary methodology of cross-track wind estimations from

92   accelerometer data as described in Liu et al. (2006). Förster et al. (2011) then presented an overview of the

93   average transpolar thermospheric circulation in terms of the vorticity. Here, they made use of the newly

94   calibrated and re-analysed data set that resulted from an ESA study, initiated for the Swarm satellites mission

95   launched in November 2013 (Helleputte et al., 2009). The CHAMP neutral wind data, based on the cross-track

96   accelerometer measurements, are available via the data repository at the GFZ Potsdam (Förster and Doornbos,

97   2019).

98

99   As pointed out by Doornbos et al. (2010), the along-track wind is not resolvable because it induces a similar

100   signal in the acceleration as the density variation. This wind component is ignored, or the value from an

101   empirical wind model is used, because the along-track wind is a relatively small magnitude in comparison with

102   the satellite speed of 7.6 km s^{-1}. The empirical wind model used is, for example, HWM90 (Hedin et al., 1991) or

103   its latest edition HWM14, as published by Drob et al. (2015). In polar areas the along-track wind velocity can

104   achieve up to 10% of the satellite speed. Consequently, the along-track mass density estimation can have an

105   error of about 20% in the polar latitudes, because the acceleration is proportional to the wind velocity squared

106   (e.g., Doornbos et al., 2010). But it is less easy to estimate the error in the cross-track wind in the polar region

107   due to considerably smaller acceleration signals. There are also systematic contributions from other sources such

108   as gas-surface interactions, surface properties, spacecraft shape, spacecraft attitude and radiation pressure

109   accelerations, which make the satellite aerodynamic coefficients difficult to resolve (see Doornbos et al., 2010,

110   and the error budget in Appendix A of that paper; Mehta et al., 2017 and March et al., 2018). The pre-processed

111   data of the accelerometer were re-sampled to 10-sec averages for the further use in this study. Measurements of

112   10-sec cadence correspond to a spatial separation of 76 km or about 2/3° in latitude between the individual data

113   points.

114

115   **3 The Fabry-Perot Interferometer data**

116   The advantage of using Fabry-Perot Interferometers is that they make direct measurements of thermospheric

117   wind speeds using only a few instrumental or geophysical assumptions. They are also generally reliable

118   instruments that can be left to run for months at a time. The FPIs operated by University College London are

119   located at the Kiruna Esrange Optical Platform System (KEOPS) in northern Sweden; and on the island of

120   Svalbard at the Adventdalen Observatory (before November 2006), from which it was moved to the Kjell
121   Henriksen Observatory (after November 2006). The geographic and geomagnetic coordinates of these two
122   stations are given in Table 1 for Kiruna (KEOPS) and Table 2 for Longyearbyen (Svalbard). The Altitude-
123   Adjusted   Corrected   Geomagnetic   Coordinates   (AACGM)   are   obtained   from
124   http://sdnet.thayer.dartmouth.edu/aacgm/aacgm_calc.php#AACGM (Shepherd, 2014). A date of 15 December
125   2002 was used, for an altitude of 240 km. Owing to the large field-of-view of the FPIs (see later) the locations of
126   the volumes observed by the FPIs in the East and West look directions are also given, and the corresponding
127   MLT.

128

129   **Table 1**

FPI Site	Geographic coordinates	AACGM geomagnetic coordinates for 15 Dec 2002 at 240 km altitude	AACGM magnetic local time (MLT) midnight in UT
Kiruna (KEOPS)	67.87°N, 21.03°E	65.08°N, 103.32°E	1.860 UT
Kiruna (KEOPS) EAST	67.87°N, 26.6°E	64.8°N, 107.8°E	2.16 UT
Kiruna (KEOPS) WEST	67.87°N, 15.5°E	65.4°N, 98.9°E	1.57 UT

130

131   **Table 2**

FPI Site	Geographic coordinates	AACGM geomagnetic coordinates for 15 Dec 2002 at 240 km altitude	AACGM magnetic local time (MLT) midnight in UT
Longyearbyen (KHO after 2006)	78.15°N, 16.04°E	75.38°N, 111.80°E	2.43 UT
Longyearbyen EAST (KHO after 2006)	78.15°N, 33.6°E	74.4°N, 123.6°E	3.21 UT
Longyearbyen WEST (KHO after 2006)	78.15°N, -1.5°E	76.8°N, 100.3°E	1.66 UT
Longyearbyen (Adventdalen before 2006)	78.19°N, 15.92°E	75.43°N, 111.80°E	2.43 UT
Longyearbyen EAST (Adventdalen before 2006)	78.19°N, 33.5°E	74.4°N, 123.6°E	3.21 UT
Longyearbyen WEST (Adventdalen before 2006)	78.19°N, -1.7°E	76.9°N, 100.3°E	1.66 UT

132

133 A significant limitation of ground based FPIs is that optical measurements of airglow and aurora at
134 thermospheric altitudes are only possible during the night when the sun's zenith angle is greater than 98°. This
135 means that the high latitude FPI observing season runs only in the winter months: from September to April at
136 KEOPS; and October to March at Longyearbyen. The FPIs have been nearly continually observing the 630 nm
137 emission from airglow and aurora every winter night since 1981 and 1986, respectively. Complete 24 hours of
138 observation are possible during November to January at Longyearbyen. Thermospheric winds have been
139 monitored by calculating the Doppler shifts of the 630nm airglow radiation intensities. The FPI instrument has a
140 mirror that rotates to look in several directions (e.g. north, north-east, east, south, west, north-west, zenith and a
141 calibration lamp) to provide line-of-sight wind measurements at a fixed elevation angle. The exposure times can
142 be as low as 10 seconds, up to 120 seconds. A typical complete scan cycle takes ~4 minutes for Kiruna and ~5
143 mins for Longyearbyen. After 1999, when laser calibrations were made possible, thermospheric temperatures
144 were measured from the thermal broadening of the emission line. More details of operation may be found in
145 Aruliah et al. (2005) and references therein.

146 The 630nm emission has a peak intensity at an altitude of around 240 km. So measurements of the Doppler
147 shifts and thermal broadening of the emission line are used to determine the winds and neutral temperatures of
148 the upper thermosphere (> 200km altitude). The elevation angle of the mirror is 45° for the Kiruna FPI and 30°
149 for the Longyearbyen FPI. Thus the radius of the field-of-view is 240 km and 416 km, respectively, which
150 represents roughly a 5° and 8° separation in latitude of the north and south viewing volumes at the respective
151 sites. At these high latitudes where the magnetospheric dynamo dominates the plasma flows, ion-neutral
152 coupling can create meso-scale structures in the upper thermosphere on horizontal scale sizes of as little as ~100
153 km (e.g. Aruliah et al., 2001). So average wind speeds have been determined for each of the 4 cardinal look
154 directions in order that the meso-scale structure is not lost. The winds are strongly dependent on UT, season,
155 solar cycle and geomagnetic activity due to the dominant forcing mechanisms of pressure gradients and ion-
156 neutral coupling in the high latitude upper thermosphere. The maximum average wind vector magnitudes
157 measured by an FPI at Kiruna were shown to be in the range 100-300 ms^{-1} and the errors of measurements were
158 around 10-20 ms^{-1} (Aruliah et al., 1996). The main sources of error are:

159   a) poor signal to noise when the 630 nm intensities are low, such as at solar minimum, or geomagnetically
160   quiet conditions.

161   b) the existence of large vertical winds. These break the assumption that the winds are predominantly
162   horizontal. Vertical winds are generally small, but can be a few 10s of ms^{-1} at high latitudes (Aruliah
163   and Rees, 1995; Ronksley, 2016). Large vertical winds introduce an error of a few per cent into the
164   calculation of a horizontal wind component from the line-of-sight measurement.

165   c) the assumption that the neutral winds are nearly constant with respect to altitude above 200 km owing
166   to the very low density and consequently high molecular viscosity of the upper thermosphere.

167

168

4 CMAT2 model winds

The UCL Coupled Middle Atmosphere Thermosphere (CMAT2) model is a 3-dimensional, time-dependent physics-based model, that solves numerically the non-linear coupled continuity equations of mass, momentum and energy (Harris et al., 2002). The model has a latitude resolution of 2°, longitude 18°, and a one third scale height for a height range of ~15 km (top of the troposphere) to 300-600km (top of the thermosphere). Thermospheric heating, photodissociation and photoionisation are calculated for solar X-ray, EUV and UV radiation between 0.1-194 nm (Fuller-Rowell, 1992; Torr et al, 1980a and 1980b; Roble, 1987). High latitude ionospheric parameters of ion and electron densities and temperatures, plus field-aligned plasma velocities, are from the Coupled Sheffield University High-latitude Ionosphere Model (Quegan et al., 1982; Fuller-Rowell et al., 1996). The high latitude auroral precipitation is provided by the TIROS/NOAA auroral precipitation model (Fuller-Rowell and Evans, 1987) and the high latitude electric field model is from Foster et al., (1986). Other features are detailed in Harris et al. (2002). The CMAT2 winds will be presented as part of the discussion below.

5. Results

Data were chosen from the 3-year periods 2001-2003 and 2005-2007, when the CHAMP satellite was in orbit. These represent periods of solar maximum and minimum, respectively. CHAMP data were collected all year around, but the FPI data were limited to nighttime periods only.

5.1 CHAMP average winds

Figures 1 and 2 show plots of average CHAMP accelerometer measurements of the cross-track thermospheric wind component during the whole period of years 2001–2003, that were obtained during direct overflights above the FPI stations at Longyearbyen (Figure 1) and KEOPS (Figure 2). The cross-track wind component is defined as pointing into the positive y-direction of the S/C coordinate system with its x axis along the orbital trace, the z axis toward nadir, and the y-axis completing the right-hand system. The y-wind component therefore points perpendicular to the orbital plane to the right side, when looking in the direction of flight. Given the high inclination (87.3°) of the CHAMP satellite, this corresponds approximately to the geographically eastward direction for the ascending orbital track (blue lines in Figure 1) except for very high geographic latitudes (see below). The cross-track wind measurements of the descending orbital tracks (red lines) have been flipped in sign to get nearly the same eastward wind component.

Figure 1a and 2a show average values for all data, while Figures 1b, 1c, 2b and 2c show the summer and winter averages. There are many more data points for the Longyearbyen station, at a higher geographic latitude compared with KEOPS. This confirms the fact that the relative probability of overhead crossings of high-latitude stations by low Earth orbiting (LEO) satellites with a near-polar circular orbit augments with increasing latitude. A statistical study has to make some compromise with respect to the area of accepted local coincidences of the satellite recordings above the ground-based observations and also with regard to the further data binning. Here, a circular area based on a 2° latitude radius and hourly bins versus local time have been used

206 which produces a sufficiently good coverage. Further binnings have been been tested to investigate the effect on
207 the results. A shorter radius deteriorates the statistics within the bin, while larger bins tend to smear the spatial
208 and temporal variations. Data filtering with respect to other parameters like, e.g., season, solar wind and
209 interplanetary magnetic field (IMF) values, solar radiation and geomagnetic activity indices should be taken into
210 account if they appear to make a significant effect.

211

212 The variance of the cross-track neutral wind magnitude is considerably larger during the whole day above the
213 station at higher latitudes. The average phase of the diurnal eastward wind variation differs also considerably
214 between the data sets of the two observatories. The eastward wind maximizes during the pre-midnight hours
215 over Longyearbyen, while a smaller maximum and a shorter interval of eastward wind is seen at lower latitudes
216 above the KEOPS station (2–3 hours versus about 6 hours). The eastward neutral thermospheric wind is
217 approximately sinusoidal for Longyearbyen (Fig. 1a), but reveals two maxima/minima over the KEOPS station
218 (Fig. 2a). The westward wind maximizes there at about 19 LT and prior to midday (~11 LT). Finally, the
219 variance of the cross-track neutral wind magnitude over the lower latitude station KEOPS is relatively large
220 during the afternoon to early nighttime hours (~15–20 LT). This might be due to the position of this station
221 relative to the large dusk cell which is known to be strongly dependent on, in particular, the IMF By component
222 (cf., e.g., Rees et al., 1986; Killeen et al., 1995; Förster et al., 2008 and Förster et al., 2011). In contrast to
223 KEOPS, the higher latitude station Longyearbyen is located close to or even poleward of the dusk cell's focus,
224 so that the cross-polar cap circulation of the neutral thermospheric air dominates.

225
226

227 **Figure 1: CHAMP observations over Longyearbyen during solar maximum 2001-2003. a) All data – ascending (blue)**

228 **and descending (red) averages; b) Summer (May-Aug) and c) Winter (end Oct-early Mar).**

229
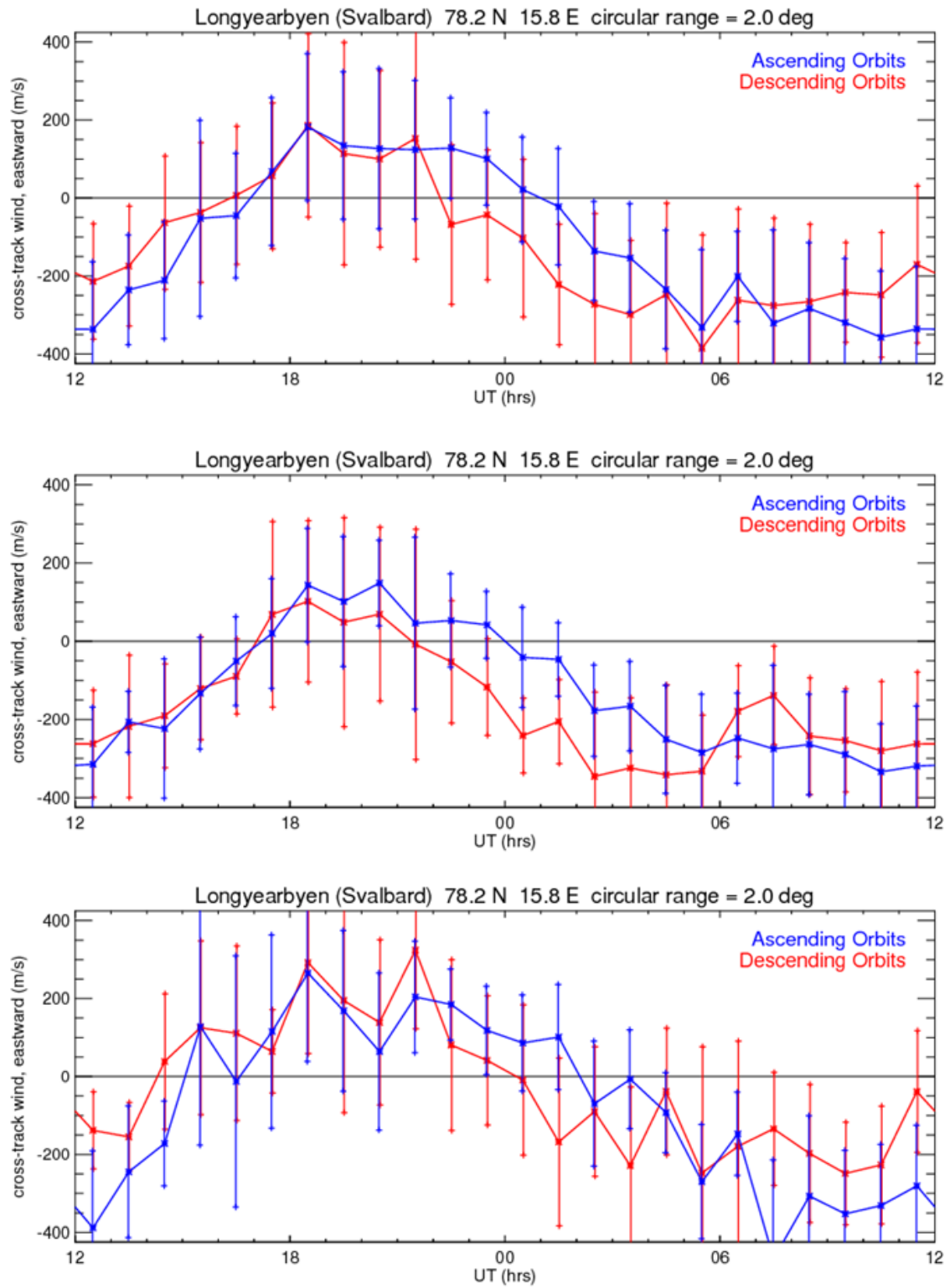
 Figure 2: CHAMP observations over KEOPS during solar maximum 2001-2003. a) All data – ascending (blue) and
descending (red) averages; b) Summer (May-Aug) and c) Winter (end Oct-early Mar).

KEOPS (ESRANGE site, Kiruna) 67.8 N 20.1 E circular range = 2.0 deg

KEOPS (ESRANGE site, Kiruna) 67.8 N 20.1 E circular range = 2.0 deg

KEOPS (ESRANGE site, Kiruna) 67.8 N 20.1 E circular range = 2.0 deg
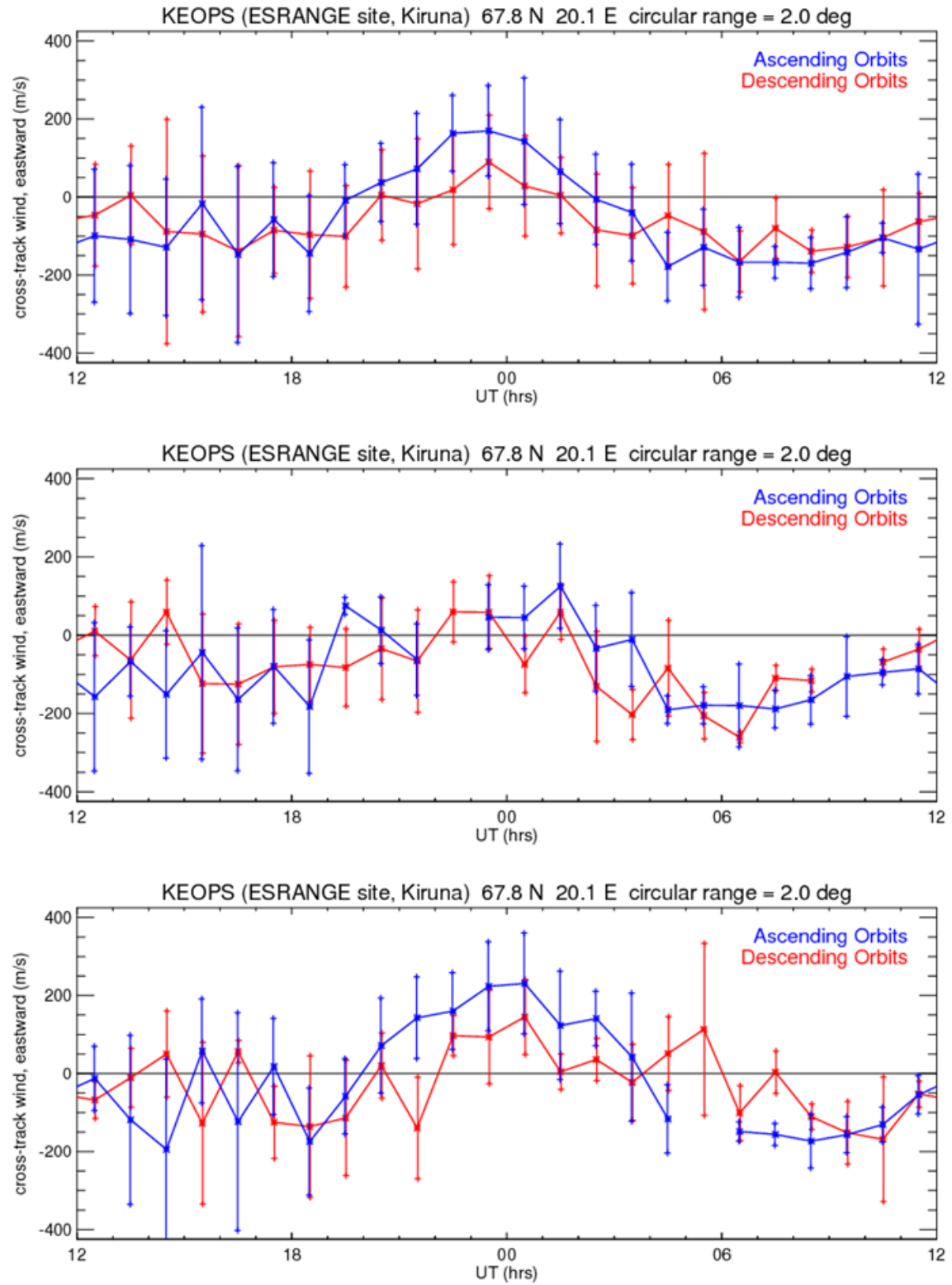
232   Figures 1b and 1c repeat the statistical plot of Fig. 1a for Longyearbyen for the years 2001-2003 with high solar

233   activity, but confined to the winter and summer months, respectively. Similarly for Figures 2b and 2c for

234   KEOPS. The statistical significance is therefore reduced, in particular for the KEOPS station, but seems to be

235   still sufficient. The winter recordings (Fig. 1c and 2c) during nighttime hours can directly be compared with the

236   FPI observations (Figs. 6 and 7).

237

238   The principle behaviour of the Longyearbyen and KEOPS eastward wind component is similar to that for the

239   full year coverage, but there are also obvious seasonal differences. The wind component amplitudes, in

240   particular the eastward maxima, are smaller during summer compared with the winter months, while the phases

241   are almost the same. The statements about the variance of the eastward/westward wind component for both

242   stations that have been made with respect to the full year statistics in Fig. 1 hold also for both winter and

243   summer plots, maybe with slightly larger values for the winter months.

244

245   The ascending and descending orbits are analyzed separately in their statistical behaviour (blue and red lines and

246   vertical bars, respectively), and show distinct differences. This points to the problem of co-alignment of the

247   ascending and descending orbital tracks (despite the simple sign flip). The small offset of ~2.7° from a strict

248   polar orbit of the satellite causes some deviation from the east/westward pointing of the cross-track

249   measurements. At low to mid-latitudes, the deviation from purely geographically eastward direction corresponds

250   in good approximation to this colatitude angle of the satellite's inclination $\beta \approx 2.7°$, but at high latitudes and in

251   particular near the poles it can deviate considerably. This non-alignment angle α (deviation from purely

252   eastward) can be estimated in dependence on the observer's colatitude θ with spherical angle relations using a

253   simplified spheric geometry of the Earth as in Eq. (1).

254

$$\alpha = \arcsin\left(\frac{\sin\beta}{\sin\theta}\right) \tag{1}$$

255

256   Using the geographic coordinates of the observatories in Table 1, one gets an α-angle of 7.2° and 13.3° for

257   KEOPS and Longyearbyen, respectively. The angular difference ($2\cdot\alpha$) between the two one-component cross-

258   track wind measurements of the ascending and descending orbital tracks is already considerable for the most

259   northward station at Longyearbyen and this offset can be noticed in, for example, Figure 1a as an offset between

260   the wind averages for ascending and descending orbital tracks during certain intervals, where the wind

261   component perpendicular to the zonal wind direction, i.e. the north-south meridional wind, is large. This is

262   obviously the case for the nighttime hours between 23–05 LT and the daytime hours between ~10–17 LT for

263   Longyearbyen and for a few nighttime hours between 23–03 LT for the KEOPS FPI station.

264

265   If the FPI technique, in particular the tri-static measurements for certain periods (Aruliah et al.,2005; Griffin et

266   al., 2008), allows the determination of specified neutral wind directions, one might consider comparing the wind

267   magnitudes for the descending and ascending orbital tracks separately for an eastward $\pm\alpha$ orientation,

268   respectively. Here, one should note, that at an observation point with an even higher geographic latitude (ideally

269   at ~86.2° geographic latitude, where the two branches of one-component observations would be perpendicular

270   to each other) it would in principle be possible to derive the full thermospheric horizontal wind vector from the

271   cross-track accelerometer measurements. This is, strictly spoken, valid in a statistical mean with characteristic

272   times of a few days, i.e. with the repetition period of ascending and descending orbits over one and the same

273   high-latitude location.

274

275   The meridional component is much larger than the zonal one during considerable periods of the nighttime

276   observation. So, to minimize the error in comparing the neutral wind magnitude, it would be better to compare

277   the full vectors. Already a small error of the measurement orientation could make a large effect on the relatively

278   small eastward wind component, which could lead us to wrong conclusions about the characteristics of the

279   differences between FPI and CHAMP accelerometer measurements. The offset between the geographic and

280   geomagnetic coordinates allows the construction of the full horizontal vector plots as statistical averages taken

281   over a period of at least 131 days of CHAMP's precession period in order to cover all local times. This

282   statistical mapping is limited to magnetic latitudes poleward of about $> 60°$ for both hemispheres (cf. Förster et

283   al., 2008).

284

285   **Figure 3: Geometry illustrating the projection of FPI look direction horizontal wind components onto the CHAMP**

286   **cross-track direction for the ascending and descending tracks.**

287
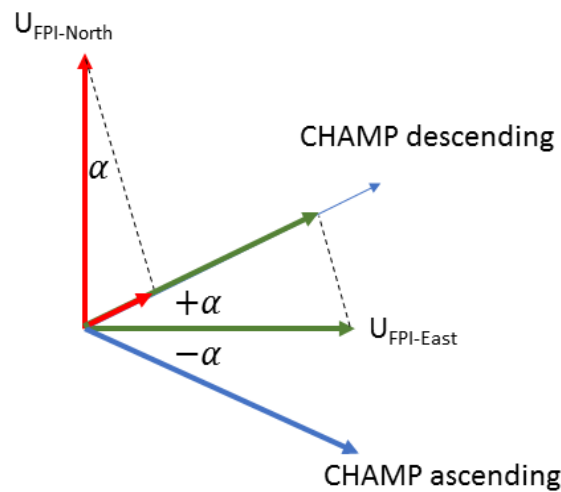
288   Figure 3 illustrates the projection of the horizontal wind component from the north and east FPI look directions

289   onto the cross-track direction of the CHAMP ascending direction. It also illustrates how the average of the

290   CHAMP ascending and descending winds gives the zonal wind component. The projections of the FPI wind

291   vectors onto each of the ascending and descending directions are used later in determining the ratio of the

292   CHAMP/FPI wind magnitudes (see section 5.2 Figure 10).

293   **Figure 4: CHAMP observations over Longyearbyen during solar minimum 2005-2007. a) All data – ascending (blue)**
294   **and descending (red) averages; b) Summer (May-Aug) and c) Winter (end Oct-early Mar).**
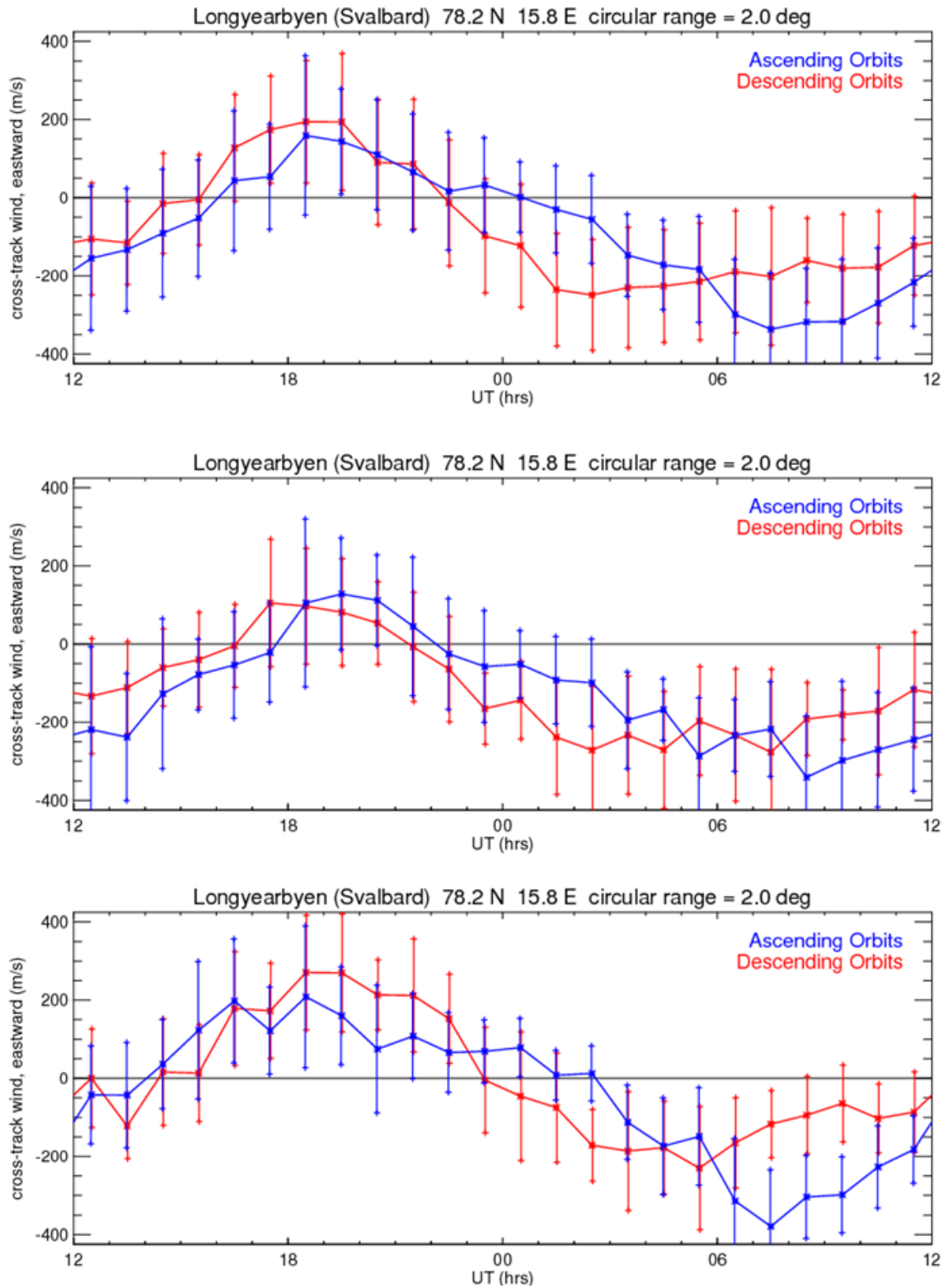
295

296 **Figure 5: CHAMP observations over KEOPS during solar minimum 2005-2007. a) All data – ascending (blue) and**
297 **descending (red) averages; b) Summer (May-Aug) and c) Winter (end Oct-early Mar).**

298
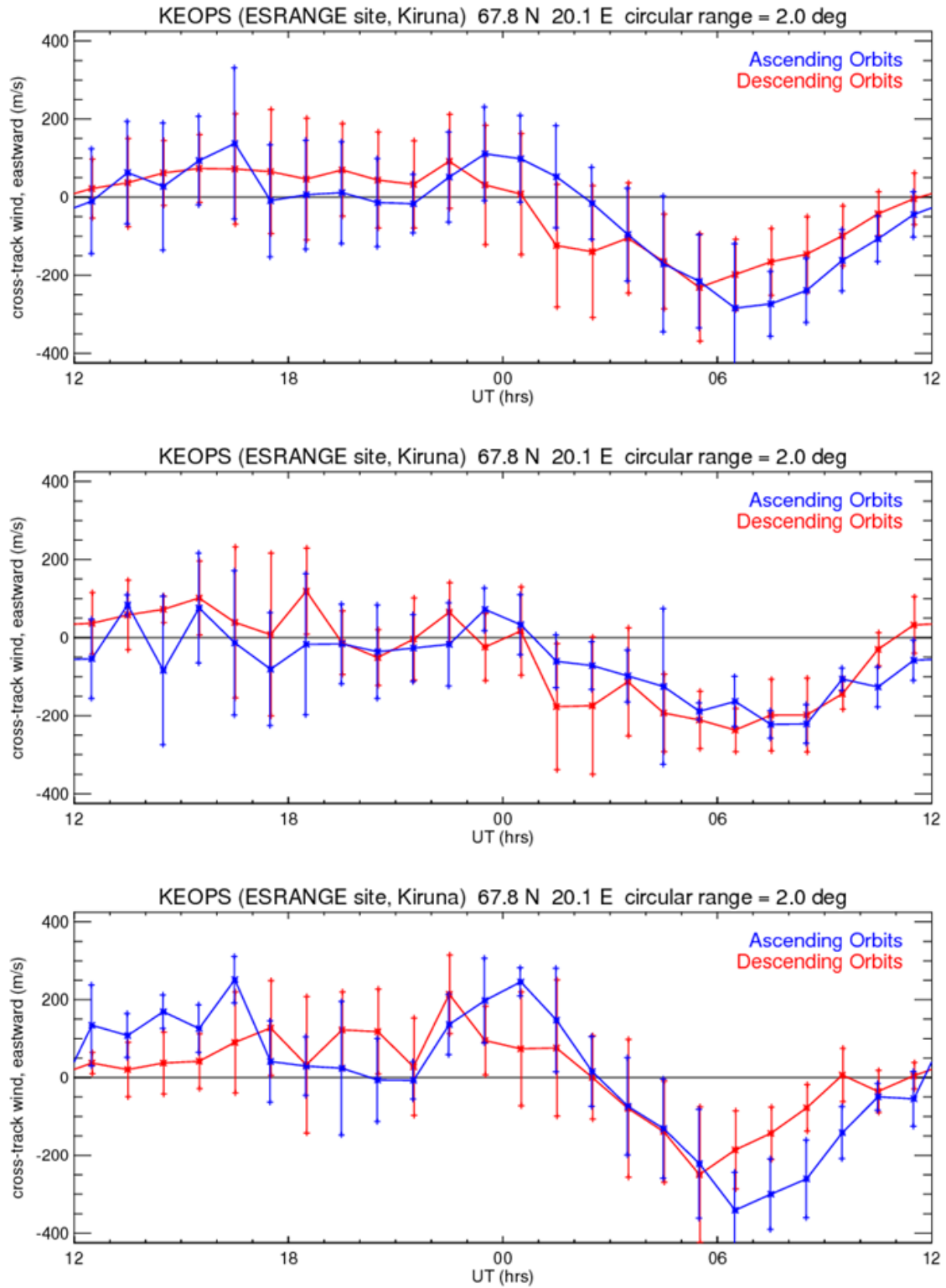
299 Figures 4 and 5 show the corresponding plots to Figs. 1 and 2, but now for low solar activity conditions during

300 the years 2005-2007. They reveal some differences as, e.g., generally smaller amplitudes and different wind

301 phases. Here, the zonal wind above KEOPS seems to point eastward during most times of the day except the

302 morning hours 04–11 LT.

303

304 **5.2 FPI average winds**

305 The average winds observed at Kiruna and Longyearbyen are presented in Figures 6 and 7. Local Time is 1 hour

306 ahead of Universal Time for both sites. The format of these figures is that the plots 6a, 6c, 7a and 7c show the

307 average zonal wind component, comparing observations from the volumes to the East and West of the site. The

308 plots 6b, 6d, 7b and 7d show the average meridional wind component from the volumes observed to the North

309 and South. The full set of cardinal direction measurements, are presented to provide a context for the

310 comparison with the zonal wind measurements made by CHAMP, especially since the CHAMP y-axis is only

311 roughly zonal. The standard error of the mean ε is added as an error bar to the FPI East and North data, where ε

312 $= \sigma/\sqrt{(N-1)}$, σ is the standard deviation and N is the number of data points. The standard errors of the mean

313 (rather than the standard deviations) demonstrate the distinctly different trends in the winds observed in the

314 volumes to the East and West of the sites, i.e. the meso-scale structure of the high-latitude thermosphere.

315 The periods of data cover the winter months of 2001-2003 and 2005-2007 to match with the CHAMP datasets.

316 The FPIs cannot measure winds during cloudy periods owing to the scatter of light by the clouds, and are only

317 able to observe the emission during the hours of darkness. Thus the observing days cannot be identical to the

318 dates when CHAMP passed overhead of the two sites. Longyearbyen has 24 hours of darkness during the

319 months of November to January, so there are nearly 24 hours of observations, but the longest period of darkness

320 at Kiruna is around 18 hours in mid-winter. CHAMP, meanwhile, is able to provide a full 24 hours of

321 observations from drag measurements.

322 There are consistent differences in the winds observed to the geographic East and West, or to the North and

323 South. This is understandable because the Kiruna site is, on average, at the equatorward edge of the auroral oval,

324 while Longyearbyen is mostly in the polar cap, though towards the poleward edge of the auroral oval. The

325 expansion and contraction of the auroral oval during an active period means that the northern half of the FPI

326 field-of-view can be very different from the southern half. In fact, Emmert et al. (2006) have shown that high

327 latitude neutral winds are better ordered in geomagnetic coordinates of magnetic latitude and magnetic local

328 time than in geographic coordinates and universal time. The AACGM geomagnetic coordinates shown in Tables

329 1 and 2 give an indication of how different are the magnetic latitudes for the East and West look directions.

330 Figure 6 shows average zonal and meridional winds from FPI observations at Longyearbyen. Figs 6a and 6b

331 show solar maximum years (2001-2003), while Figs 6c and 6d show solar minimum years (2005-2007). Figs 6a

332 and 6c show the zonal winds to the East and West using the convention of +East, while Figure 6b and 6d shows

333 the meridional winds to the North and South, using +North. The average standard deviations σ are ±103 ms^{-1}

334 and ±64 ms^{-1} for the solar maximum zonal and meridional winds, respectively.

335

336 Figs 6a and b show solar maximum (2001-2003) FPI winter average wind components at Longyearbyen for
337 geomagnetically quiet conditions ($0 \leq$ Kp < 2-). a) Zonal and b) meridional average winds and the standard errors of
338 the mean are plotted. North and East are purple lines, while South and West are light blue.

339
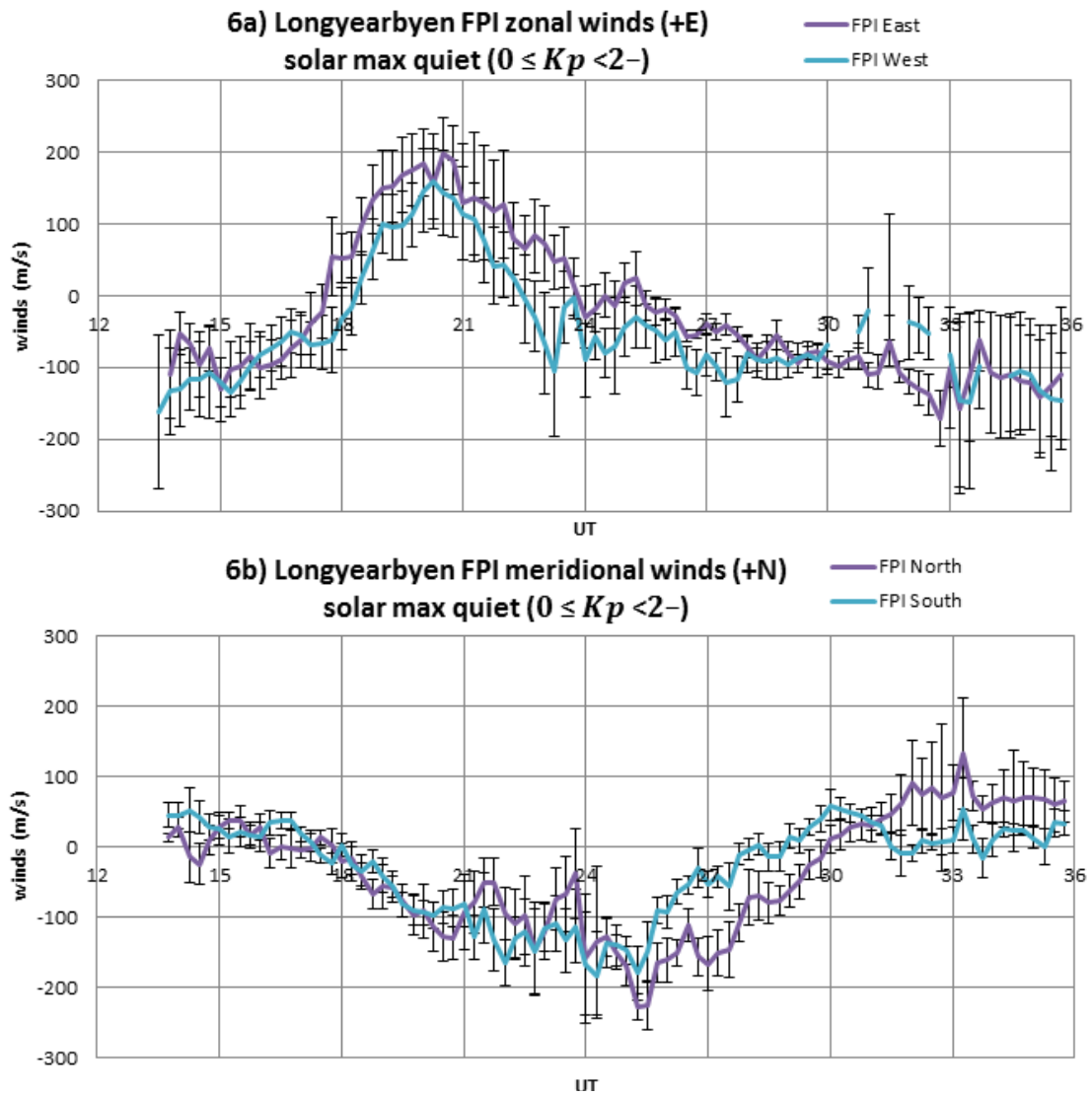
340   **Fig 6c and d show solar minimum (2005-2007) FPI winter average wind components at Longyearbyen for**

341   **geomagnetically quiet conditions ($0 \leq \mathrm{Kp} < 2$-). a) Zonal and b) meridional average winds and the standard errors of**

342   **the mean are plotted. North and East are purple lines, while South and West are light blue.**

343

344
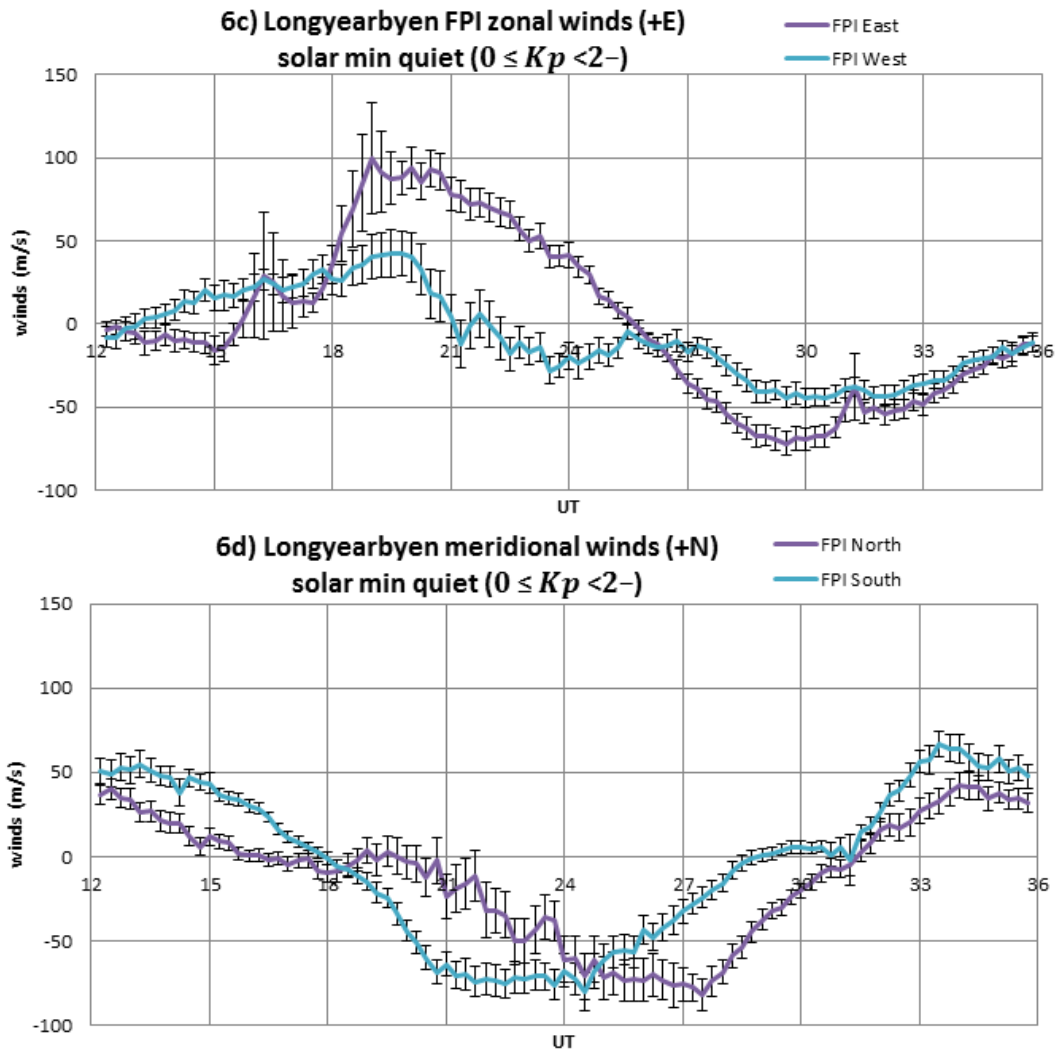
Longyearbyen is just within the polar cap. The winds are predominantly antisunward despite the geomagnetic activity level, since this is the direction for both the pressure gradient and ionospheric convection. As a result, Longyearbyen observations are a somewhat less obvious indicator of ion-neutral coupling behaviour than observations at KEOPS in the period 1800-2100 UT. The Longyearbyen solar maximum (2001-2003) winter winds (day numbers 300-65), during geomagnetically quiet conditions ($0 \leq Kp < 2$-) are shown in Figures 6a and 6b. The zonal winds (Figure 6a) show westward winds before 1800 UT and then eastward winds for ~6 hours which then turn westward. The maximum wind speed is about 200 ms^{-1} eastward between 1800-2400 UT. The meridional winds (Figure 6b) are slightly northward before 1700 UT, then turn southward until 0600 UT, and return northward. The maximum speed is about 200 ms^{-1} southward at about 0100 UT. The standard errors of the mean are around ± 30 ms^{-1}, however the values vary systematically through the night. Between 1800-2100 UT the standard error is around 3 times larger than between 0300-0900 UT when it is very small.

Figures 6c and 6d show the Longyearbyen FPI winds for clear nights during winter (DOY 300-65) 2005-2007, geomagnetically quiet conditions ($0 \leq Kp < 2$-). There is a full 24 hours of observations in this dataset, and the extreme quiet of this solar minimum period has provided a large number of observations for this category. The antisunward flow appears clearly. There is a strong phase lag between the observations to the North and South. This is puzzling because it cannot be explained in terms of ordering high latitude winds in geomagnetic coordinates. This category is for the most geomagnetically quiet conditions possible: solar minimum during a prolonged solar minimum, and the lowest Kp values. Under these conditions the geographic coordinate system under which the solar flux heating operates, should be the most appropriate. The average standard deviations are ± 55 ms^{-1} and ± 47 ms^{-1} for the zonal and meridional winds, respectively. The standard errors of the mean are very small, averaging less than ± 10 ms^{-1}, though again there is a clear systematic UT-dependent trend. Between 2100-0300 UT the standard error of the meridional wind is about 2-3 times larger than at other times. Between 1500-2000 UT the zonal wind standard error becomes considerably larger.

369 **Fig 7a and b show solar maximum (2001-2003) FPI winter average wind components at KEOPS for geomagnetically**

370 **quiet conditions (0 ≤ Kp < 2o). a) Zonal and b) meridional average winds and the standard errors of the mean are**

371 **plotted. North and East are purple lines, while South and West are light blue.**

372

373
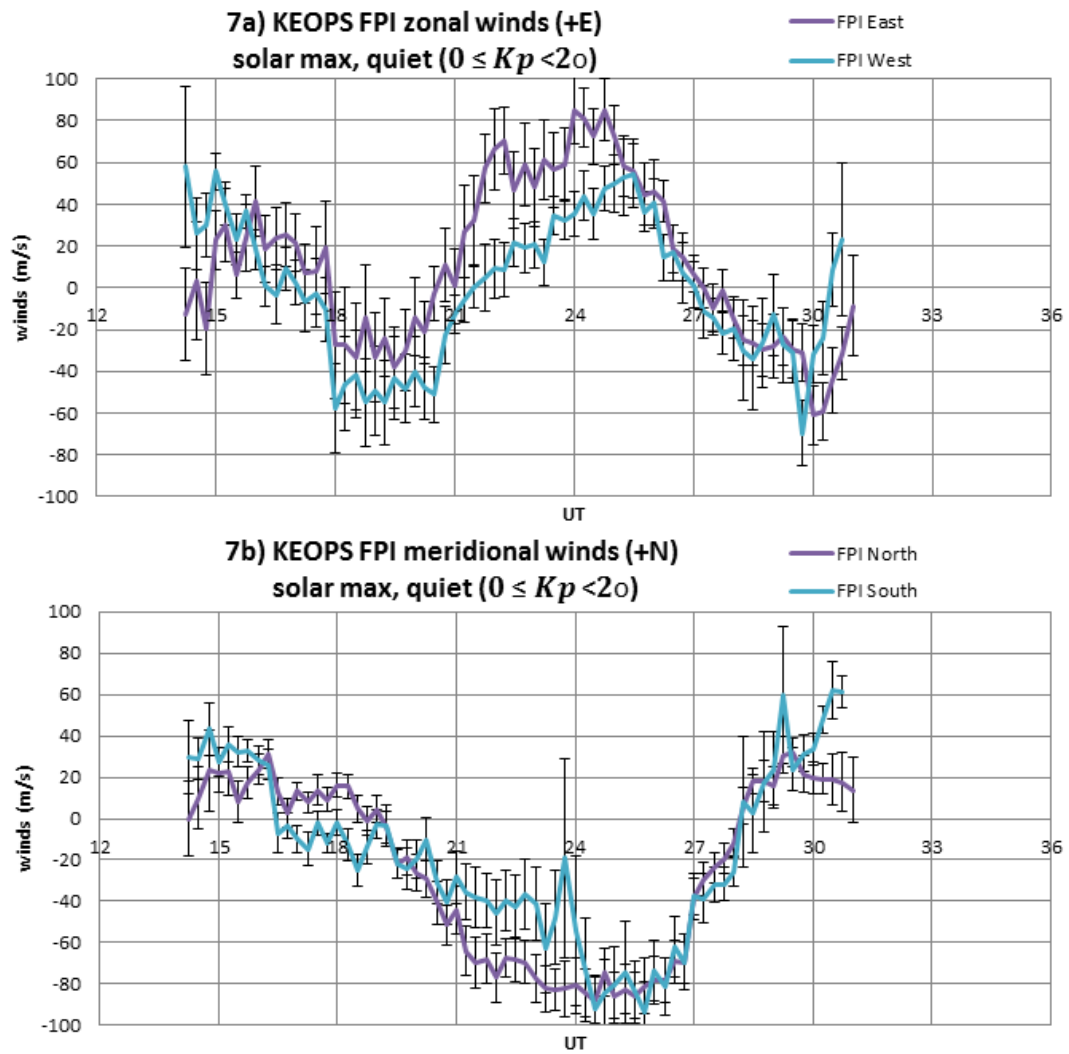
374   **Fig 7 c and d show solar minimum (2005-2007) FPI winter average wind components at KEOPS for geomagnetically**

375   **quiet conditions** $(0 \leq Kp < 2\text{-})$**. a) Zonal and b) meridional average winds and the standard errors of the mean are**

376   **plotted. North and East are purple lines, while South and West are light blue.**

377
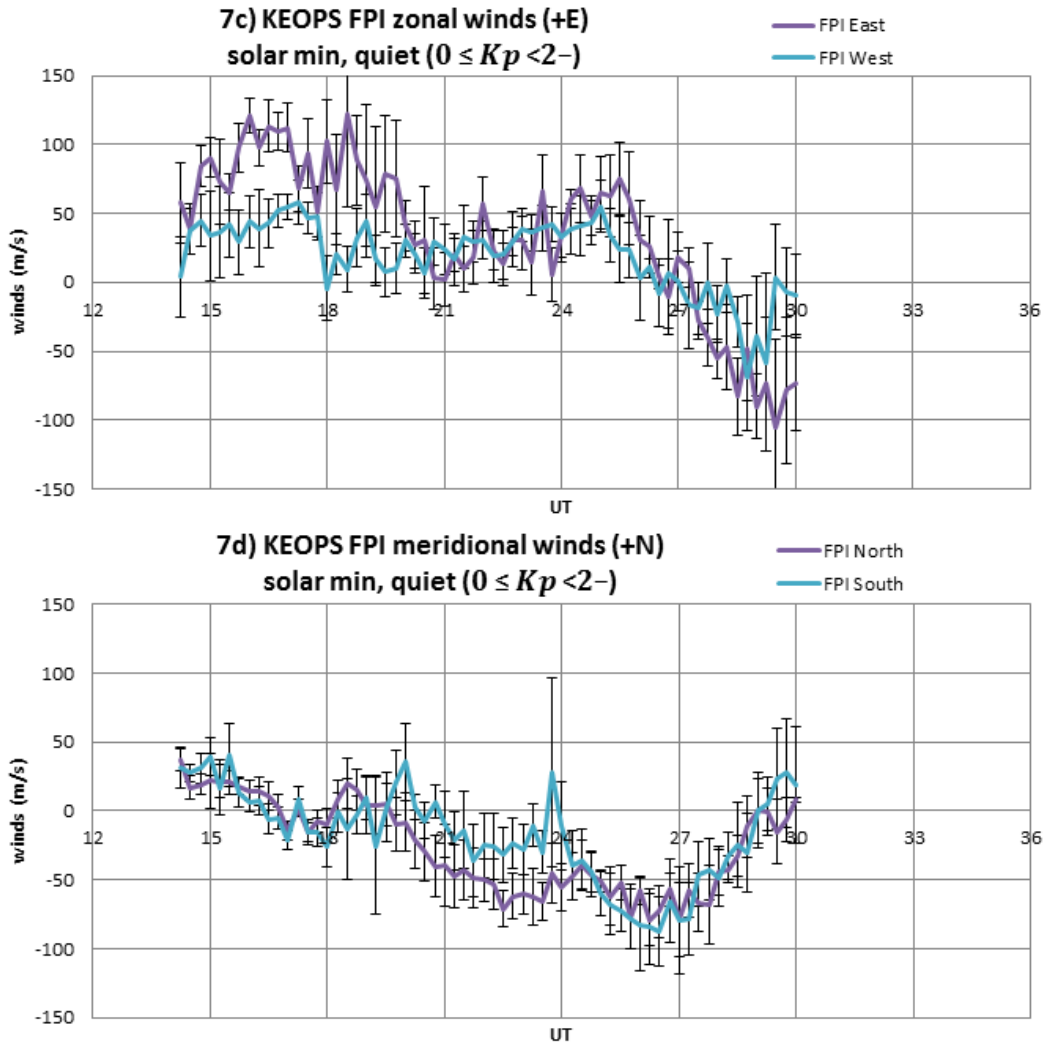
378   Figure 7 shows the KEOPS FPI winds for clear nights during winter (DOY 300-65) during geomagnetically

379   quiet conditions. The general diurnal trends are similar for both solar maximum (Figs 7a, b) and minimum (Figs

380   7c, d). The solar minimum data range is $0 \leq Kp < 2\text{-}$, but it was necessary to increase the geomagnetic activity

381   spread for the solar maximum data to improve the statistics, so Figures 7a, b show $0 \leq Kp < 2o$. The meridional

382   winds show antisunward flow that is predominantly driven by the pressure gradient from dayside EUV heating,

383   resulting in fairly weak southward winds reaching a maximum value of nearly 100 ms^{-1}. The standard errors of

384   the mean are around ±10-15 ms^{-1}. The zonal winds are eastward before 1800UT, reaching a maximum speed of

385   a few 10s ms^{-1}. After 1800 UT the zonal winds turn westward for a few hours and back eastwards around

386   2100UT. Between 2100-0300 UT the zonal winds reach their maximum speed of up to 80 ms^{-1} before turning

387   westward again. The zonal winds are more variable, and their standard errors of the mean are slightly larger than

388   for the meridional winds, averaging 16 ms^{-1}.

389   The few hours of westward flowing zonal winds during 1800-2100 UT are particularly interesting (Figs 7a and

390   7c). The westward flow indicates that the winds are briefly under the influence of the clockwise dusk cell of

391   ionospheric convection. Through collisions between the ions and neutral gas, momentum is transferred to the

392   neutrals, which diverts them from the direction of the pressure gradient driven anti-sunward/eastward flow. The

393   action of the centrifugal force balancing the Coriolis force keeps the winds entrained in the cell (Fuller-Rowell

394   and Rees, 1984). As the KEOPS site passes under the region of the Harang Discontinuity (Harang, 1946), the

395   FPI West zonal winds turn back to eastward about 40 mins after the FPI East zonal winds. This is because the

396   KEOPS FPI East observing volume is a horizontal distance of 480 km away from the FPI West volume (note

397   that the distance between the viewing volumes depends on the altitude of the 630 nm emission). However, note

398   that at the latitude of KEOPS, the time taken for the Earth to rotate through a distance of 480 km is 46 mins. The

399   difference between 40 min and 46 min is partly due to the difference in magnetic latitude. It is also due to the

400   Harang Discontinuity being dependent on the IMF B$_y$ orientation, resulting in a smearing out of the MLT

401   interval.

402   Figures 7c and 7d show the KEOPS FPI winds for clear nights for the years 2005-2007 during winter (day

403   numbers 300-65), geomagnetically quiet conditions (0 ≤ Kp < 2-). These years were during the unusually

404   extended solar minimum of the last solar cycle when the solar flux levels were extremely low, and observations

405   of aurora were rare. Consequently the plasma density was smaller, and the thermosphere was more compressed,

406   resulting in smaller neutral densities at a given height. Under these conditions the ion drag driver is less

407   efficient, and the pressure gradients, together with the Coriolis and centrifugal forces, play a larger role. Thus,

408   although the trends are similar to the solar maximum winds; the zonal winds are strongly eastward throughout

409   the evening sector. There are no westward zonal winds until after 0300 UT, and generally the wind amplitudes

410   are smaller. The maximum meridional wind is about 80 ms^{-1} southward around 0300 UT. The maximum zonal

411   winds are seen to the East, and these are around 100 ms^{-1} eastward in the evening sector and start to increase

412   westwards towards 100 ms^{-1} by 0600 UT. The average standard errors of the mean are around ± 20 ms^{-1}, which

413   are larger than for solar maximum conditions.

414   The general trends seen in the northern winter geomagnetically quiet CHAMP zonal winds (Figures 1-2, and 4-

415   5) are also seen in the FPI winds (Figures 6-7). The phases match well for both sites, however, there is a

416   considerable difference in magnitude. The next two figures (Figures 8-9) show direct comparisons of CHAMP

417   and FPI winds along the cross-track direction for moderately active conditions (2$^-$ ≤ Kp < 4$^+$). There is a lot of

418   modelling effort into studying the active ionosphere-thermosphere, which makes this comparison useful. In

419   particular it is relevant to the argument in section 6.4 where CHAMP and FPI neutral winds are compared with

420   typical ion velocities actively observed by ground-based radars at high latitudes.

421

Fig 8 Longyearbyen (Svalbard) winters 2001-2003, 2- ≤ Kp < 4+: average zonal winds measured using CHAMP and FPI, including standard errors of the mean. These are compared with FPI winds observed by the University of Alaska in 1980, and the HWM93 model winds.
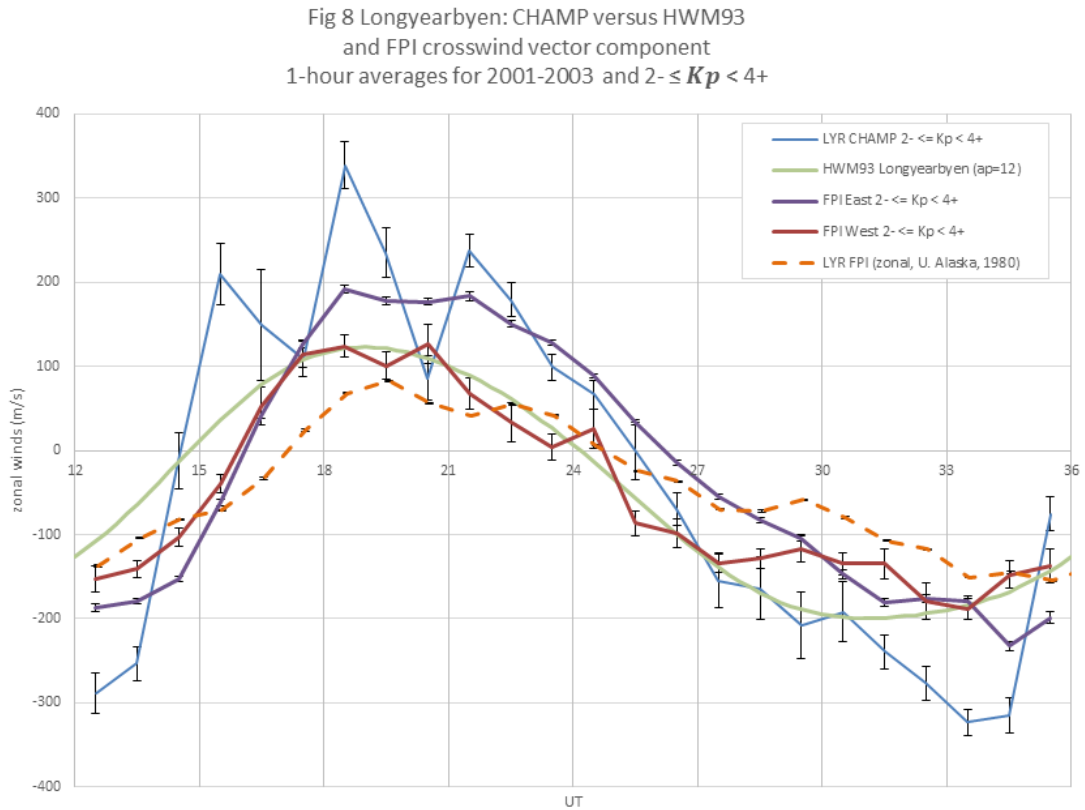
Figure 8 is a direct comparison between CHAMP cross-track winds at Longyearbyen and several different sources. The winds represent moderately active conditions (2⁻ ≤ Kp < 4⁺) during winter months (DOY 300-65) for solar maximum years. The HMW93 model conditions are for the 31st December with ap = 12 (Kp = 3-); F10.7 =150; height 400 km (Hedin et al., 1996). At Longyearbyen there can be 24-hour coverage by the FPI owing to continual darkness between November-January. The direct comparison is made by projecting the components of the FPI and HMW93 (Hedin et al., 1996) wind vectors along the CHAMP ascending and descending cross-track directions using $\alpha = \pm 13.3°$. CHAMP cross-track winds and UCL Longyearbyen FPI observations are averages for 2001-2003 (a failure occurred in the rotating mirror mechanism in late December 2003 so CHAMP 2004 data were not included). The data are then the averages of the ascending and descending components to give a zonal wind.

FPI wind values taken from Figure 9 in the paper by Hedin et al. (1991) are also plotted. These values are measurements from the University of Alaska FPI that collected Longyearbyen data in 1980, 1981 and 1983. The aim is to demonstrate that the FPI technique of measuring Doppler shifts gives consistent results, which is discussed in section 6.2. The U.Alaska FPI winds were an average of the East and West look directions, justified by the assumption of a uniform horizontal wind field over the field of view. This was a common practice at that time owing to a) the assumption of a large molecular viscosity of the thermosphere which reduces wind shear,

and b) the longer exposure times of the earlier FPIs (6-12 minutes) which used photomultipliers with piezoelectrical scanning of the FPI etalon gap size in order to view the full Free Spectral Range (Deehr et al., 1980). The UCL FPIs were amongst the first FPIs to use fixed gap etalons to image the full FSR onto a 2D array of pixels. This allowed shorter exposure times, and a rapid cycle of look directions, which consequently revealed mesoscale spatial and temporal structures of the order of a few 100 km horizontally and minutes (e.g. Aruliah and Griffin, 2001, Aruliah et al, 2005). During the 1980s and 1990s we used state-of-the-art UCL designed and built Imaging Photon Detectors (McWhirter et al., 1982). Astrocam Antares cameras replaced the IPD in the Svalbard FPI from 1998, and in the KEOPS 630 nm FPI in 2002. However, these cameras had the disadvantage of slow readout times which were essential for the best noise performance and so time resolution was compromised. In 2003 the first Electron Multiplying CCDs revolutionised low light level imaging. These cameras combined superior signal to noise ratio with very fast readout times. The first one was put into service at KEOPS in 2003, followed by Svalbard in 2005 (McWhirter, 2008). The huge advancement over the last 30 years in low light detectors has allowed atmospheric gravity wave observations using exposure times as little as 10 seconds at auroral latitudes (Ford et al., 2007). Note that the upgrade of the detector is to improve the photon sensitivity which reduces the error of measurement. It does not change the calibration of the wind speeds.

Any changes of etalon required re-calibration of the measured Doppler shift to calculate winds, as discussed in section 6.2. The KEOPS FPI used a 10 mm etalon gap up to January 2002, when it was replaced with an 18.5 mm gap etalon. Then in January 2003 a 14 mm etalon was put in, which has been there until the present time. For the Longyearbyen FPI there was a 14 mm etalon until April 2005, which was replaced with an 18.5 mm etalon from September 2005 until the present time.

All sources show generally similar phases, with peak eastward winds in the evening sector, between 18-24UT and westward winds in the morning sector, between 06-12UT, as expected for anti-sunward flows. Table 2 shows that the AACGM MLT for Longyearbyen is about 2.4 ($\pm$ 0.8 for the East and West volumes) hours ahead, so magnetic midnight is approximately at 21.6 UT. The standard errors of the mean are plotted for all data. The U.Alaska Longyearbyen FPI standard deviations are around $\pm$ 150 ms^{-1}, which are similar to the UCL FPI. For the purposes of comparison, a standard error of $\pm$ 30 ms^{-1} is plotted for the U.Alaska FPI data, similar to the average UCL FPI standard error. It was noted in the Hedin et al (1991) paper that for both hemispheres, the average high latitude winds from the FPIs at Sondrestrom, Longyearbyen and College in the northern hemisphere, and Mawson in the southern hemisphere, showed a systematically smaller diurnal variation than the DE 2 mass spectrometer data. The more recent measurements from CHAMP and the UCL FPI are clearly typically different in magnitude, but consistent with the trend noticed by Hedin et al (1991). The diurnal amplitude of the UCL zonal winds is about 170 ms^{-1}, and for the U.Alaska winds is about 125 ms^{-1}. The CHAMP zonal winds are the largest in magnitude, with a diurnal amplitude of around 300 ms^{-1}.

The average of the monthly F10.7 fluxes is 184 for the winter periods Nov-Feb of 1980-81, 1981-82 and 1983-84, and 160 for the winters of 2001-2003. Yet despite the higher average solar flux in 1980, the UCL FPI zonal wind magnitudes have a significantly larger amplitude than the U.Alaska zonal winds. Closer inspection of the 3 winter periods of 2001-2003 shows a spike in the average monthly F10.7 for November 2001-February 2002 (i.e. <F10.7> is 214 for Nov-Feb 2001-2002; 145 for Nov-Feb 2002-2003; and 123 for Nov-Dec 2003) which

481   may account for the 3 winter average UCL FPI winds being larger than for U.Alaska. The geomagnetic activity

482   levels are similar, averaging Kp values in the range 3⁻ to 3º for all three winters. These are interannual and inter-

483   solar cycle discussions for a later paper.

484

485   **Fig 9 Comparison of CHAMP and FPI measurements of KEOPS zonal average winds to the FPI East and West**

486   **volumes, including standard errors of the mean, for winters 2001-2003. These are compared the HWM93 model**

487   **winds.**

488

489
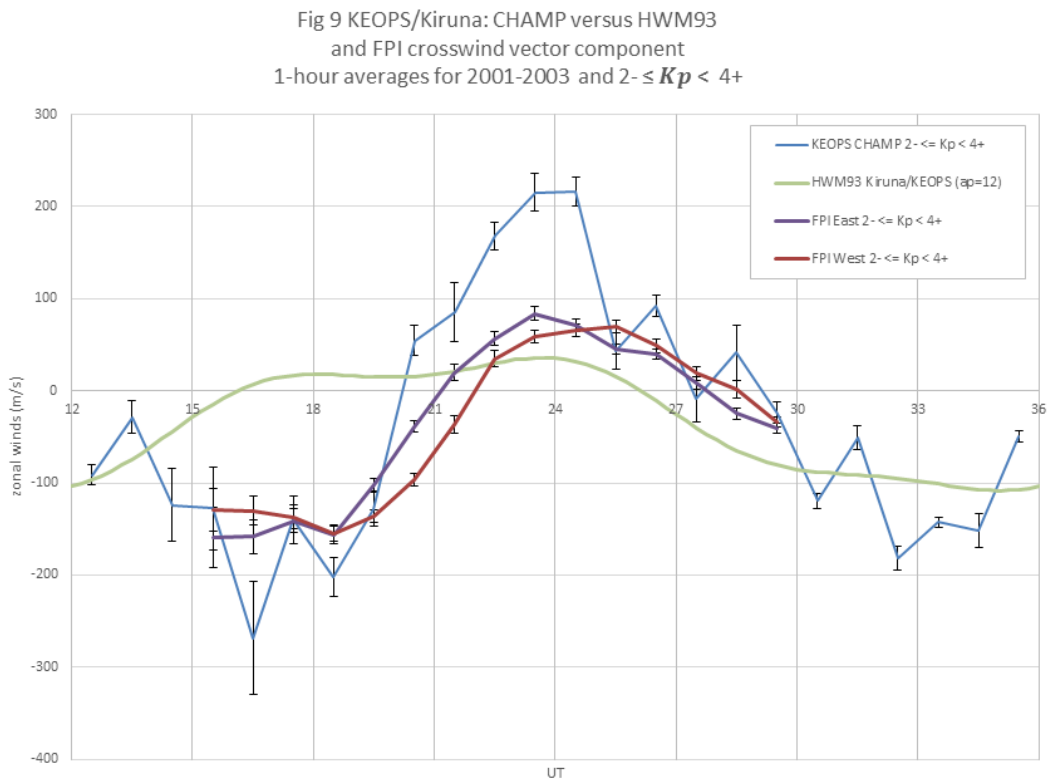
490   Figure 9 shows a comparison of the CHAMP zonal winds against the UCL FPI winds at Kiruna/KEOPS for the

491   solar maximum winters of 2001-2003. The FPI and CHAMP data are selected for moderately active conditions

492   ($2^- \leq$ Kp < 4^+) as in Figure 8. At Kiruna the hours of darkness are between 15-06UT for the period November-

493   January. The direct comparison is made by taking the component of FPI and HMW93 (Hedin et al., 1996) wind

494   vectors in the CHAMP cross-track direction using $\alpha = \pm 7.2°$. The UCL FPI average zonal winds for $2^- \leq$ Kp

495   < 4+ are shown separately for the East and West look directions. There is a smaller difference between these

496   look directions than for the Longyearbyen zonal winds. The evening winds for moderately active solar

497   maximum conditions are around -150 ms⁻¹ (westward), and reach a peak of around 70 ms⁻¹ (eastward) in the

498   midnight sector. The AACGM MLT for Kiruna is about 1.9 (± 0.3 for the East and West volumes) hours ahead,

499   so magnetic midnight is approximately at 22.1 UT, which is the time separating the period of the evening

eastward electrojet and the morning westward electrojet in magnetic local time coordinates. The behaviour of the zonal winds shows strong ion-neutral coupling for these moderately active conditions, so that there is a semidiurnal variation representative of the twin cell ionospheric convection pattern at auroral latitudes. This is in addition to the day-night diurnal variation of winds driven by the pressure gradient.

The phase of the CHAMP zonal winds is in good agreement, but the amplitude is considerably larger. The peak evening wind reaches -200 ms^{-1} (westward) and 200 ms^{-1} (eastward) by 02 UT. What is particularly interesting about this comparison is the difference between the CHAMP and FPI winds in the period 15-20 UT. The CHAMP winds are considerably less westward, and are more similar to FPI average zonal winds for geomagnetically quieter conditions at solar maximum, as shown in Figure 7a. The large standard error of the mean during the period 15-20 UT shows how sensitive the winds are to ion drag within the dusk cell.

Figure 10a shows the histogram of the frequency distribution of the ratios of CHAMP/FPI 1-hour averaged cross-track zonal wind magnitudes from Figures 7 and 8. Figure 10b shows the UT dependence. The Longyearbyen ratios cluster in the range 1.0 - 2.5, while the Kiruna ratios are far more widely spread. Overall there is a general trend for the satellite wind magnitudes to be larger by a factor of 1.5 - 2.0, with median values of 1.7 for Longyearbyen (24 hours coverage) and 1.3 for Kiruna (1530-0530 UT coverage). There does not seem to be any clear pattern when the UT-dependent frequencies of the ratios are plotted in Fig 10b, except for a tendency for the more extreme ratios to occur during the midnight period, when the 630 nm emission is weakest, and the FPI winds have the largest error bars. Even if the midnight measurements are excluded, there is a wide range of values generally greater than 1.0.

Fig 10a, b Frequency distribution of the ratios of CHAMP/FPI one-hour averaged zonal wind magnitudes observed in the winter period for solar max under moderately active conditions (2- ≤ Kp < 4+) for Longyearbyen (blue) and KEOPS (red). Fig 10a shows the frequency distribution of the CHAMP/FPI ratios, and Fig 10b shows the UT dependence of the ratios.
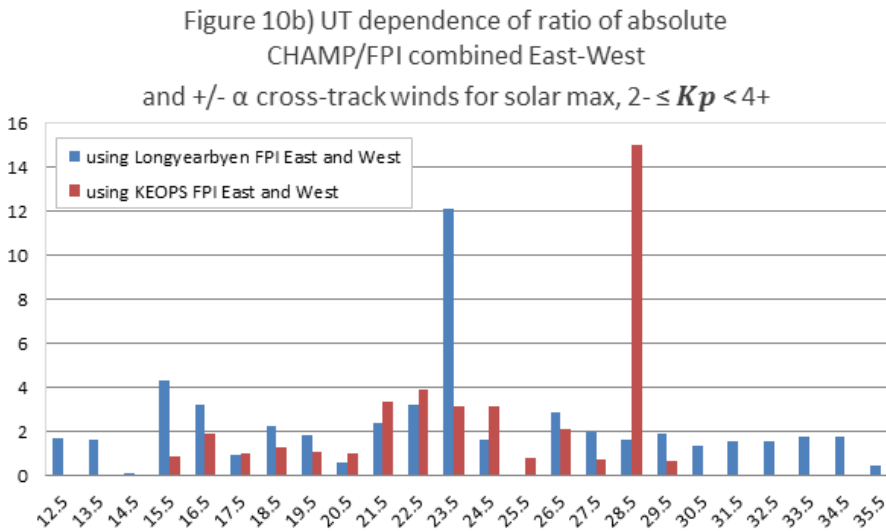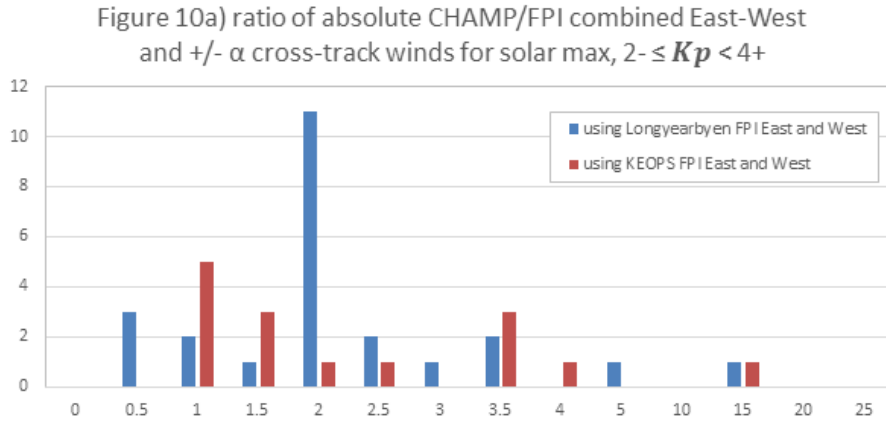
6. Discussion

We have shown that there is a similar phase, but a considerable difference between the average zonal wind magnitudes measured by the CHAMP satellite and the ground-based FPIs for a polar cap and auroral site during northern winter months. Our premise is that the large molecular viscosity of the upper thermosphere should minimise any vertical structure in the winds above around 250 km altitude. The difference in wind magnitudes could have various explanations. It could be that A) we are mistaken about the vertical structure of winds; or B) that there is a problem with the scaling of the two methods of measurement; or C) the measurement procedures introduce differences, e.g. in-situ versus remote integration; comparison of different spatial and/or temporal resolutions. There may be other, unexpected, reasons for the mainly amplitude differences in the measurements.

With respect to hypothesis A: the CHAMP satellite zonal winds are of a similar magnitude to the original GOCE satellite winds (Liu et al., 2016 and Visser et al., 2019), and to the UCL CMAT2 model simulations. However, while the CHAMP satellite altitude was between 350-400 km, the GOCE satellite had an unusually low altitude around 250 km, which was close to the FPI 630 nm emission peak altitude. The CMAT2 winds are typical of values from other GCMs, which were largely calibrated against measurements by satellites in the 1970s and 1980s, in particular the DE-2 satellites. Killeen et al (1984) found a good agreement between the FPI at Longyearbyen (then called the University of Ulster FPI, and subsequently the University of Alaska FPI) for observations in December 1981. Though later Hedin et al. (1991) found that on average the satellite wind measurements were larger. The DE-2 satellite measurements were made using the Wind and Temperature Spectrometer (WATS), rather than derived from satellite drag measurements. The DE-2 satellite flew from August 1981 to February 1983, which means that the average monthly F10.7 flux included some of the highest solar flux values of the last 30 years. This may account for why physical and empirical GCMs calibrated from that period have such large wind values. The two decades since 2000 have recorded the most sustained and low F10.7 flux levels since the satellite era began.

With respect to hypothesis B: the satellite drag community are already aware of a scaling issue. Defining the drag coefficient is the largest source of error. Bruinsma et al (2014) had to multiply GOCE densities by a factor of 1.29 to match the real-time High Accuracy Satellite Drag Model (Storz et al., 2005). HASDM uses data assimilation from the orbits of 75-85 inactive payloads and debris over 200-900 km altitude that are tracked by the Space Surveillance Network (SSN) and is considered a benchmark by that community. Recently March et al. (2019), reanalysed thermospheric densities derived from very precise satellite accelerometers and GPS acceleration using high fidelity satellite geometries. The densities for all the spacecraft surveyed were greater than those derived using surfaces defined by flat panels; and more consistent with each other. The CHAMP and GOCE densities were found to be 11% and 9% larger. Although there is no simple link between densities and winds, this re-scaling of densities gives an indication that it may be necessary to scale winds down for the same measured acceleration (see section 6.3 and Eq. 6).

With respect to hypothesis C – the assumptions of the FPI and CHAMP measurement techniques are discussed in the following sections 6.1-6.3.

6.1 Considering the molecular viscosity of the upper thermosphere

Let us first consider hypothesis A, that the CHAMP and ground-based FPI average zonal measurements are both correct, and that the factor of 1.5-2.0 difference in wind magnitudes is due to the 100-150 km difference in the altitude of the measurements. Conventional fluid dynamics theory predicts that the molecular viscosity is very high in the upper thermosphere owing to the very low particle densities at these altitudes. The viscosity of a fluid determines how resistant it is to shear forces that cause adjacent layers to move at different speeds. Turbulent viscosity dominates the atmosphere below about 100 km, but molecular viscosity dominates the upper atmosphere. The molecular viscosity of the upper thermosphere is very large, and in the CMAT2 model the molecular viscosity η, is given by Eq. (2) (Harris, 2001; Hood, 2018) which is based on Dalgarno and Smith (1962).

570
$$\eta = 4.5e^{-5} \times \left(\frac{T}{1000} \right)^{0.71} \qquad (2)$$

571   As a consequence of large viscosity, there is little shear between the different altitude layers above ~200 km for
572   both winds and neutral temperatures (hence the name thermosphere representing an iso-thermal behaviour). The
573   issue raised in this paper is that the difference between CHAMP and FPI wind magnitudes is too large to be
574   consistent with the assumption of large viscosity over this range of altitudes.

575

576 **Fig 11 CMAT2 zonally averaged zonal winds for 00UT at December solstice 2008 (solar minimum conditions) to**
577 **demonstrate the effect of drastically reducing the molecular viscosity in order to raise the altitude where winds**
578 **become independent of altitude. The left panel shows isobars for a standard simulation, while the right panel**
579 **represents a simulation where the molecular viscosity is 100 times smaller (from Hood, 2018).**
580
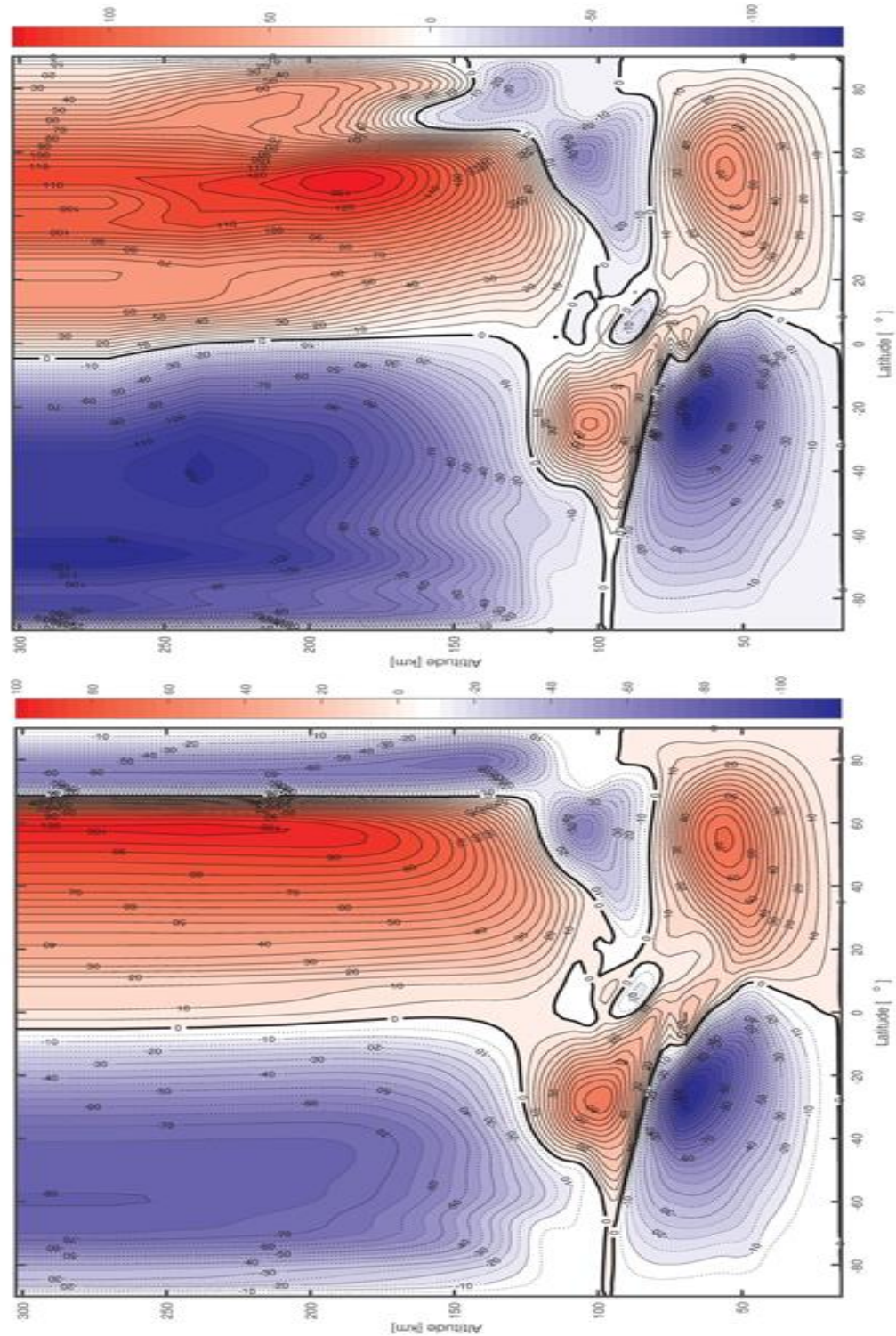
581   Figure 11 shows two versions of the CMAT2 zonally averaged zonal winds for 00 UT for December solstice

582   2008 (solar minimum conditions) from Hood (2019). These are latitude-height plots, where the height is from

583   15 km to 300 km. From about 250 km the contour lines become near vertical because the large molecular

584   viscosity of the upper thermosphere minimises the shear in the winds. The left hand plot is the standard run

585   using standard values of molecular viscosity. The right hand plot shows the contours for a simulation where the

586   molecular viscosity has been reduced by a factor of 100. The variation of the molecular viscosity with respect to

587   temperature (and consequently height for our purposes) has been tested theoretically and experimentally by

588   Dalgarno and Smith (1962), and the factor of 100 is an unrealistic extreme used to test the model. The

589   consequence is that the height at which contours become vertical is raised to closer to 280 km. This is a small

590   difference and certainly does not account for the apparent vertical gradient indicated by the difference between

591   the CHAMP and FPI zonal winds.

592   Song et al. (2009) state that the fastest acceleration of the neutrals occurs near 350 km in the F layer, where the

593   effective neutral-ion collision frequency maximizes (see their Figs. 6 and 7). Considering the dynamic character

594   of frequent changes of the IMF and the magnetospheric convection, the stronger accelerations at F2 layer

595   heights could result in temporary vertical neutral wind gradients. However, the 1-D model approach neglects

596   forces due to neutral pressure and effective molecular viscosity in the 3-D continuum of the upper thermosphere.

597   To describe correctly the long-range coupling on time scales from longer than few seconds to less than 30 min,

598   the inductive effect (Faraday's law) as well as the dynamic effect of the neutrals, in particular (acceleration

599   terms), need to be considered (Song and Vasyliunas, 2013). This poses a challenge for future modelling efforts

600   of the M-I-T system.

601   Recently Vadas and Crowley (2017) published results from observations of 10 Travelling Ionospheric

602   Disturbances at ~283 km altitude, observed in 2007 with the TIDDBIT ionospheric sounder near Wallops

603   Island, USA. They used ray tracing on the TIDs and simultaneously measured a peak in the neutral wind at ~325

604   km altitude using a sounding rocket. They found a serious discrepancy between where the gravity waves were

605   predicted to dump energy using conventional dissipative theory, and the observations from TIDDBIT and the

606   rocket. Conventional theory predicted that all the gravity waves should have dispersed at a scale height below

607   the rocket measurement. Consequently they have challenged convention and proposed that the molecular

608   viscosity should not increase as rapidly with altitude above 220 km. This may account for some of the difference

609   between the CHAMP and FPI zonal winds, but will need to be tested in future modelling studies.

610

611   **6.2 FPI Doppler shift to wind speed procedure**

612   Hypothesis B is that the FPI and/or CHAMP observations may need to be re-scaled. To start with the FPIs we

613   will look at the calculation of the Doppler shift and then at the height integration procedure of a ground-based

614   FPI.

615   The calculation of the wind speed requires few assumptions, though the process of fitting the FPI fringes is more

616   complicated (e.g. Makela et al., 2011). The wind speed u is determined from the Doppler shift of the wavelength

617    $\Delta\lambda$ of the moving volume of gas which emits at wavelength λ, where the free-space wavelength is λ_o and the

618   speed of light c (Eq. 3).

619
$$\lambda = \lambda_o \left(1 + \frac{u}{c}\right) = \lambda_o + \Delta\lambda \tag{3}$$

620   The speed of the volume of gas u is given by Eq. (4), which is proportional to the ratio of the Doppler shift in

621   fringe peak position (in bins) Δx; and the free spectral range (FSR), Δx_{FSR}. The FSR is the equivalent wavelength

622   shift to re-position a fringe from overlapping one order of the baseline wavelength λ_o, to the next order. The

623   other terms in Eq. (4) are the refractive index μ of the medium between the etalon plates and the separation of

624   the plates, d (Hecht and Zajak, 1980).

625
$$u = \left(\frac{\Delta x}{\Delta x_{FSR}}\right)\left(\frac{c\lambda_o}{2\mu d}\right) \tag{4}$$

626   The etalon gap is evacuated so $\mu=1$, and the other parameters are known. Thus for example, for an etalon gap d

627   = 10 mm, emission λ_o = 630 nm, free spectral range Δx_{FSR} = 150 bins, a Doppler shift of 1 bin (Δx = 1 bin)

628   would represent a wind of 63 ms^{-1}.

629   All the parameters for the scaling of the FPI winds in this equation are known. There is the issue of determining

630   the zero Doppler shift baseline because there is no laboratory source of the excited atomic oxygen. However, the

631   method used to determine the baseline (i.e., using a helium-neon source with the assumption that the vertical

632   component of the wind is negligible) introduces an average systematic offset error of at most 10-20 ms^{-1}, which

633   is small compared with horizontal wind magnitudes (Aruliah and Rees, 1995).

634

635 **Fig 12 left: height profile of CMAT2 zonal winds at Svalbard. Right: height profile of the red line emission intensity**
636 **profile from the Vlasov et al (2005) model.**
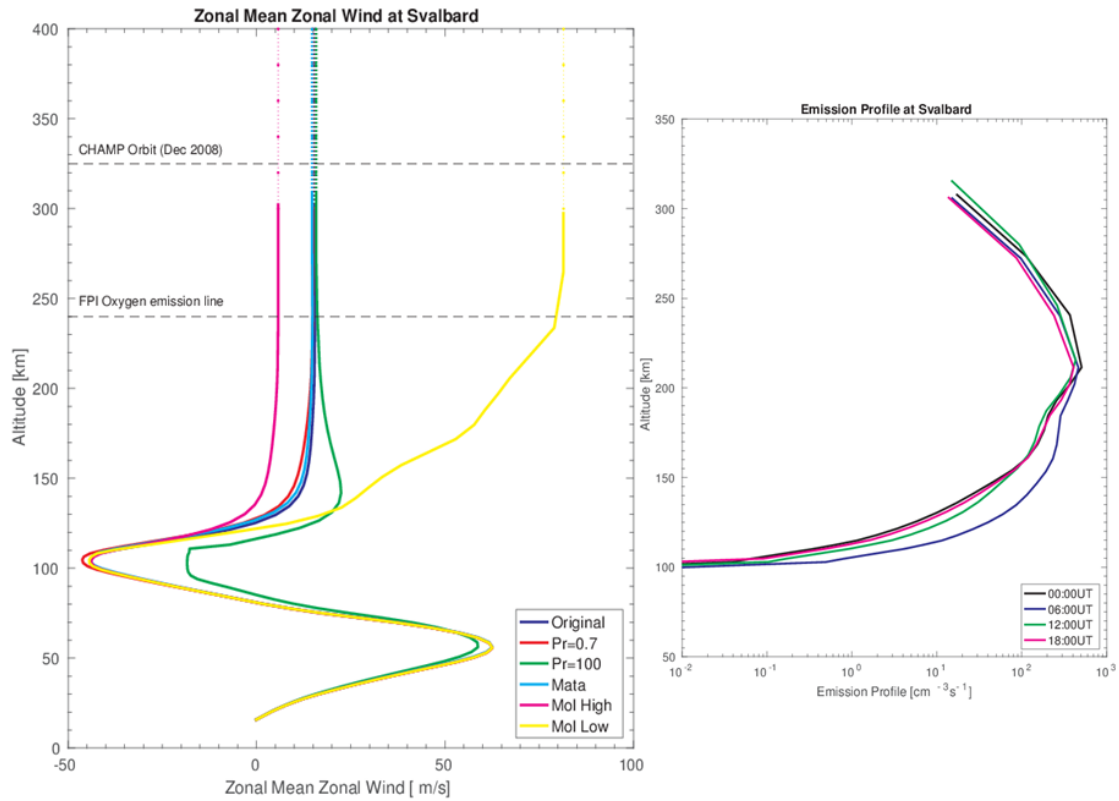
637 Figure 12 illustrates how ground-based FPIs make measurements of the neutral winds at 240 km altitude. The
638 left plot shows a height profile of the CMAT2 zonal mean zonal winds at the latitude of Longyearbyen. There
639 are 6 simulations to demonstrate the effect on the height profile of the zonal mean zonal winds when changing
640 the viscosity. CMAT2 uses a viscosity term that is the weighted mean divided by the scale height of two
641 coefficients of viscosity: the molecular viscosity μ_m; and the turbulent viscosity μ_t. The simulations represent a
642 comparison with the original molecular viscosity (dark blue). The other lines are for low (yellow - divided by
643 100) and high molecular viscosities (pink - doubled). The low and high turbulent viscosities are represented by
644 the Prandtl numbers 0.7 (red) and 100 (green), where 2 is the default value used in CMAT2. The Prandtl number
645 is related to the height at which gravity waves deposit momentum (Liu et al., 2013) and so may have relevance
646 for the Vadas and Crowley experiment (2017). The light blue line labelled "Mata" is an intermediate profile. As
647 can be seen, the molecular viscosity dominates in the thermosphere above 100 km and at the altitudes where the
648 FPI is measuring. The dark blue and yellow lines are representative of a vertical slice of Figure 11 left and right,
649 respectively, for the latitude of Longyearbyen.

650 The right hand plot of Figure 12 is a CMAT2 height profile of the 630 nm (red) line emission intensity based on
651 the Vlasov et al. (2005) model at 00UT, 06UT, 12UT and 18UT. The red line emission at night is dominated by
652 dissociative recombination of molecular oxygen ($O_2^+ + e \rightarrow O^* + O$). The altitude distribution of the 630 nm
653 emission has a peak emission altitude of between 220-250 km. However, the emission profile also has a full

width at half maximum intensity of around 50-70 km, i.e. sampling altitudes tens of km below and above the emission peak. The ground-based FPI observes a height-integration of the emission along the line-of-sight. The measured Doppler shift is therefore an integration of the Doppler shifts at all altitudes, weighted by the emission profile. However, there are several reasons to justify why we are confident that the FPI provides a good sample of the winds at ~240 km altitude. The excited atomic oxygen state in the O (^{1}D-^{3}P) transition is a forbidden transition with a long life-time of ~110 sec (Bauer, 1973), which allows the excited atoms to thermalise before emission and be representative of the surrounding gas. Below 200 km the molecular composition increases significantly, and the long lifetime means that the 630 nm emission is quenched due to molecular collisions with N_2 and O_2. Consequently we can assume there is minimal contribution of Doppler shifts from below 200 km altitude, which is a region where the neutral wind magnitude has a large height dependence (note that the emission intensity x-axis is a log scale; and that the horizontal winds at 100 km altitude are a few tens of ms^{-1} while at 250 km altitude are a few hundreds of ms^{-1}). Above the altitude of the emission peak the flux falls off rapidly with altitude, and also with distance from the FPI, which minimises the contribution of winds from the region above. In addition, above 250 km the wind magnitudes begin to reach an asymptote. It therefore would be expected that the satellites and ground-based FPIs should see very similar speeds and phases. With respect to the FPI measured winds, the contribution of winds below the peak emission height may result in a small underestimate of the winds at ~240 km altitude, which is investigated later in this section by modelling.

The tristatic FPI experiments by Aruliah et al (2005) and bistatic experiments by Anderson et al (2012) indicated that the winds, neutral temperatures and 630 nm intensities were closely matched if the geometry assumed an emission altitude of around 240 km. However, during auroral activity, when there is E-region precipitation, the red line emission altitude can be lower, perhaps as low as 200 km. This means that the FPI samples lower altitudes. Recently Gillies et al. (2017) used all-sky imagers to triangulate the peak emission height of the 630 nm emission. They found that discrete auroral arcs showed a characteristic height of 200km. The effect of particle precipitation in lowering the emission height was earlier noted by Sica et al. (1986). They illustrated how decreased thermospheric temperatures measured by a Fabry-Perot spectrometer at College, Alaska, were consistent with lower MSIS temperatures (Hedin et al., 1977) when weighted by a modelled emission height profile. However, aurorae are limited to high latitudes and occur infrequently as illustrated by Figure 13, which shows the frequency distributions of Kp values for the years (top) 2001-2003 representing solar maximum; and (bottom) 2000-2009, i.e., for most of the period of the CHAMP lifetime. Aurora generally occur during active periods when Kp > 4-5. Thus emission heights of 200 km are the exception rather than the rule, and affect the average only minimally.

685 **Fig 13 Frequency distribution of Kp values. Top: 2001-2003 representing solar maximum. Bottom: 2000-2009**
686 **covering most of the period of the CHAMP lifetime.**
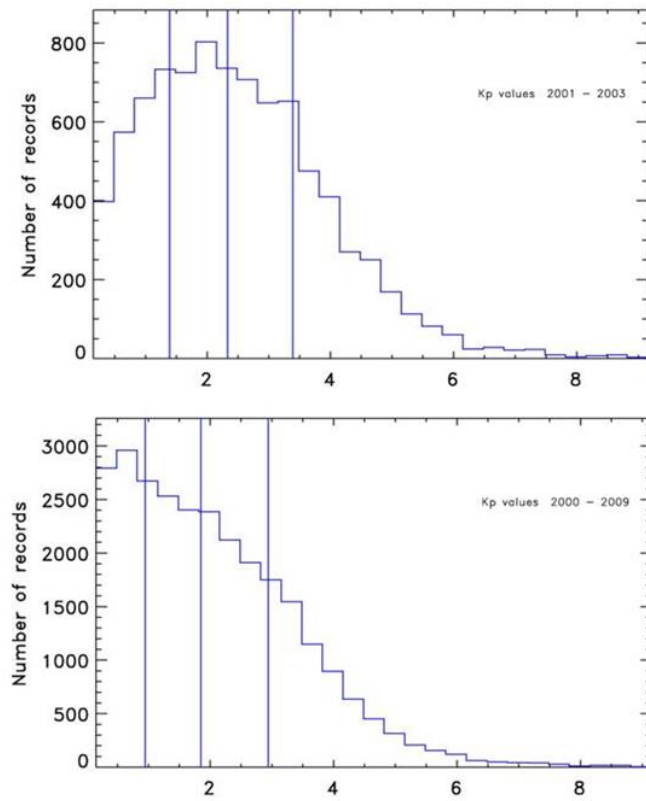
687 **Fig 14 top: CMAT2 zonally averaged zonal winds for a quiet day on 1st December 2007 at Longyearbyen (left) and**
688 **Kiruna (right) for the winds at 180, 200 and 240km for comparison with the height integrated winds weighted using**
689 **an emission intensity profile from the Vlasov et al (2005) model. Bottom: the same for active conditions on 20th March**
690 **2015.**

691
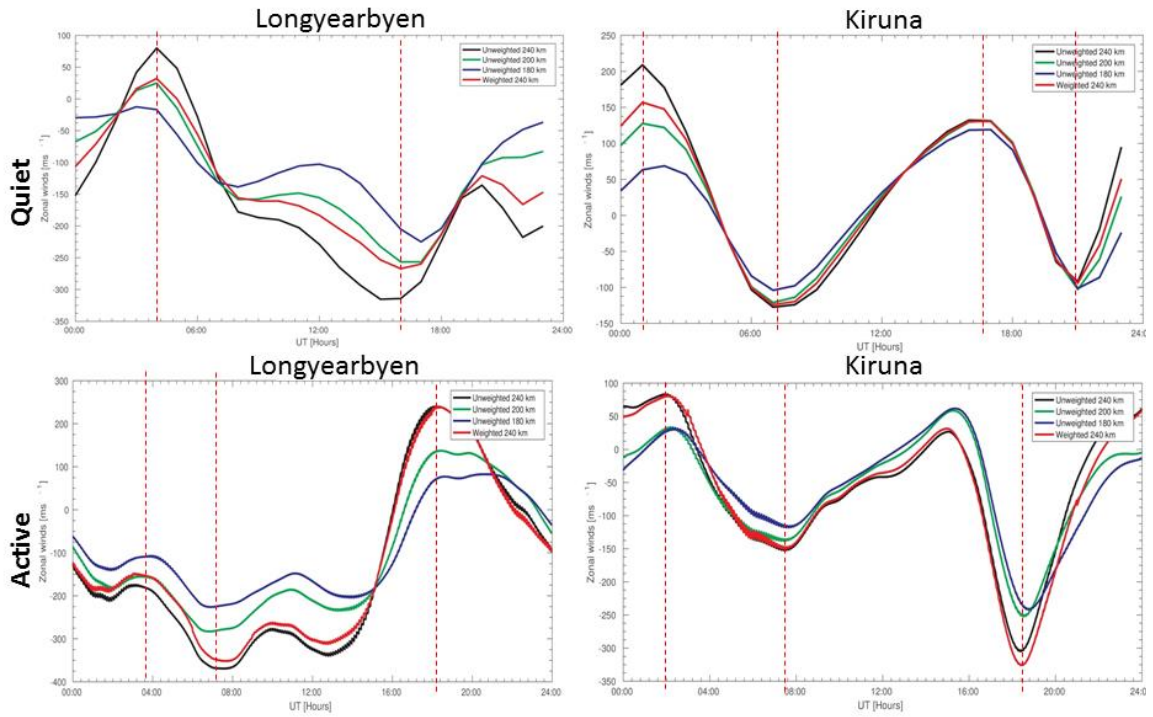
692 In order to assess by how much the FPI height integration method is underestimating winds, CMAT2 winds at

693 240 km are compared to a column integration average of CMAT2 winds weighted by the emission intensity

694 profile. Here the Vlasov et al (2005) model is applied with constants provided by Yiu (2014), and with CMAT2

695 winds interpolated to 10 km intervals for the integration. Figure 14 compares the CMAT2 zonally averaged

696 zonal winds at three heights: 180 (blue), 200 (green) and 240 km (black) with height integrated winds (red) for a

697 quiet day run on the 1st December 2007 (top panels) and an active day run on the 20th March 2015 (bottom

698 panels) for both Longyearbyen (left column) and Kiruna (right column). Figure 15 outlines the CMAT2 model

699 global view of the unweighted and weighted winds at 240km for 00, 06, 12 and 18UT.

700

Fig 15: CMAT2 global zonal winds for a quiet day on 1ˢᵗ December 2007 for the winds at 240km and the height integrated winds weighted using an emission profile from Vlasov et al (2005) model. From top left: 0UT, 6UT. From bottom left: 12UT, 18UT.
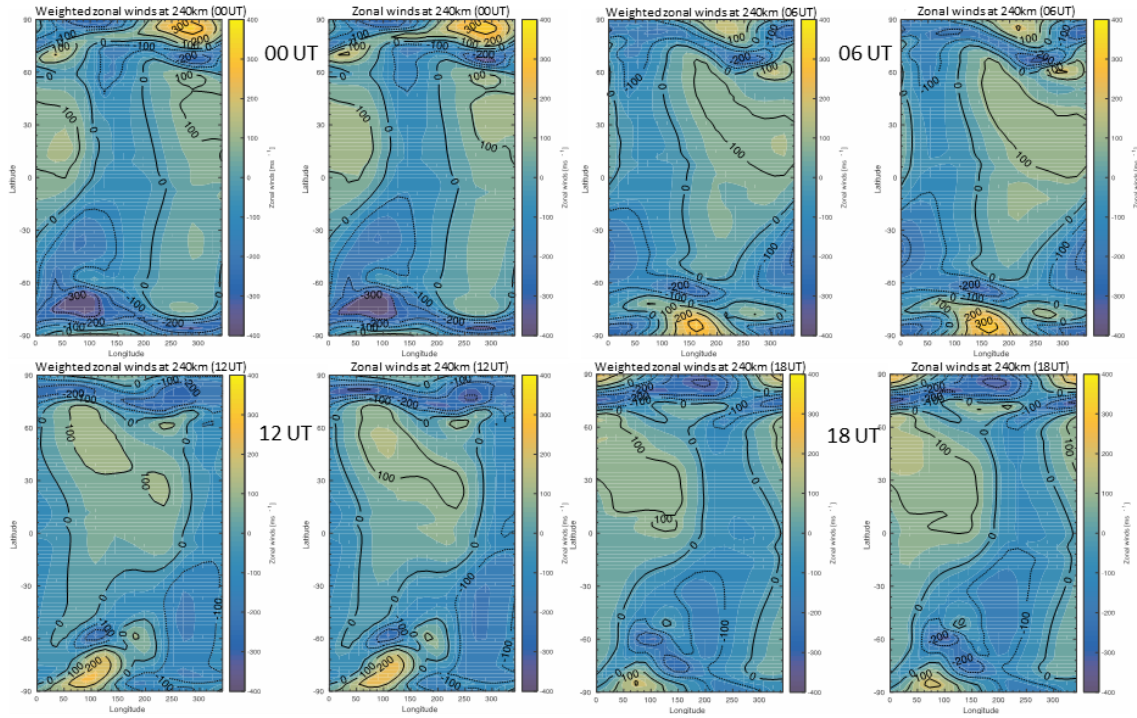
Figure 14 indicates that there are some significant differences between zonally averaged zonal winds with or without height integration. The lower the altitude, the smaller the wind magnitude. There is also a slight change in phase (to aid the eye these are indicated by vertical dashed lines placed at turning points for the weighted winds). This is due to the increased collision frequency at lower altitudes due to greater density, and the consequent shift in balance between pressure gradient and ion drag. When we look at the averaged diurnal variation of the CHAMP and FPI winds, their phases are almost exactly the same. This would not be the case if the FPI was observing winds dominated by Doppler shifts at 190 km altitude, where the phase would be significantly different because the pressure gradient increases its dominance at lower altitudes. Comparing the CMAT2 December 2007 model zonally averaged zonal winds at 240 km with the height integrated winds, the most significant difference is for Longyearbyen during quiet conditions, which on calculating overall mean values produces a 19% difference, that during active conditions reduces to a difference of 12%. The reverse seems the case for Kiruna as the mean percentage difference increases from 3% to 14% between the quiet and active days respectively. Note that the wind speed scales are different for each panel. For each time-series there is no simple systematic trend. Figure 15 demonstrates these dissimilarities on a global scale; here the zonal winds appear to be slightly more westward, as the eastward winds are diminished and the westward winds enhanced. However, this is not the case for all times of day shown here, and does not visibly affect the wind distributions to any large extent.

6.3 CHAMP cross track wind procedure

Satellites have provided global coverage of accelerometer measurements since 2001, in particular, the CHAMP satellite (e.g. Schlegel et al., 2005) and GRACE satellites (e.g. Tapley et al., 2004). These measurements of satellite drag have been converted to measurements of thermospheric mass density (e.g. Liu et al., 2005) and cross-track thermospheric wind measurements (e.g. Sutton et al, 2007, Liu et al., 2006, Förster et al., 2008). Thermospheric mass density was primarily estimated using Eq. 5 where $\underline{a}$ is the satellite acceleration, ρ the neutral mass density of the air, C_d refers to a dimensionless drag coefficient, using a constant frontal area A_{ref} of the satellite with mass m, and total velocity V relative to the atmosphere in the ram direction given by the unit vector $\hat{\underline{v}}$. This equation has been used for a first simple cross-track wind estimation, where the area and wind component were replaced by the horizontal side view and neutral wind direction perpendicular to the bulk flow, respectively.

$$\underline{a} = -\frac{1}{2}\rho \frac{C_d}{m} A_{ref} V^2 \hat{\underline{v}} \tag{5}$$

For the first analysis, Liu et al. (2005) explained that they used a fixed drag coefficient value of $C_d = 2.2$. This is a de-facto standard value used for compact satellite orbit computations since the 1960s (e.g. Cook, 1965). This value was adopted by Jacchia when constructing his thermosphere density model, based on physical drag modelling of spherical satellites (Jacchia and Slowey, 1972). The drag coefficient is acknowledged to be very difficult to quantify, as is discussed extensively by, for example, Moe et al. (1995). The importance of the value of C_d is acknowledged by Liu et al (2006) and others who use the data, since it affects the scaling of the density and wind calculations. However, their interest was in the relative density and wind structures, rather than absolute values.

Since then the analysis has been refined considerably by taking into account lift, sideways, as well as drag forces on the satellite, resulting in smaller wind magnitudes as described by Doornbos et al. (2010). The GOCE satellite winds are closer in magnitude to ground-based FPI measurements (Dhadly et al., 2017), though still systematically larger in magnitude, where the difference has been found to increase with latitude. The systematic residual line-of-sight GOCE wind varied between 20 ms^{-1} at 50° MLAT to a maximum 150 ms^{-1} at 85° MLAT (see Figure 2 from Dhadly et al., 2018).

Another consideration is that CHAMP measures the cross-track wind component (Figures 1-2 and 3-4) which deviates from the pure zonal direction as measured by the FPIs (Figures 6 and 7). The geometry can be critical, in particular for the high-latitude Longyearbyen FPI, because the cross-track deviates from the zonal direction by about 13.3° in each direction respectively for the ascending and descending orbits. The meridional wind component at these high latitudes is much larger than the zonal one, so that the larger CHAMP measurements at this FPI could also (at least partially) be due to an "admixture" of the meridional wind component and the zonal wind. This has been discussed in section 5.1 to account for the difference between the average zonal winds measured during the ascending and descending orbits. To deal with this the UCL FPI zonal winds observed to the East and West are projected onto the CHAMP ascending and descending cross-track directions, and then averaged into 1-hour bins, thus replicating the CHAMP zonal wind averages (see Figures 7 and 8). Despite this

759 re-calculation there is a wide range of values of the CHAMP/FPI ratios (see Figure 10a, b), which reinforces the

760 message that the satellite aerodynamic coefficients are difficult to determine absolutely, which is in addition to

761 some systematic factor between the CHAMP and FPI measurements.

762

6.4 Comparison with EISCAT radar ion velocities

764 Finally, a very important consideration is how the average winds compare with ion velocities. At high latitudes

765 the ion velocities are generally larger than the neutral winds owing to the $\underline{E}$ x $\underline{B}$ drift driven by the

766 magnetospheric electric field. Davies et al (1995) provided a statistical analysis of E- and F- region ion

767 velocities observed on 20 March 1996 in order to compare measurements by the EISCAT incoherent scatter

768 radars and the CUTLASS coherent scatter radar. The scatter plot of ion velocities from this study (their Figure

769 5) indicated a cluster of values in the range of a few hundred ms^{-1}, with only a small fraction of measurements

770 greater than 500 ms^{-1}.

771 Fiori et al (2016) compared ion velocities measured by the Electric Field Instrument on Swarm with the CS10

772 statistical ionospheric convection model by Cousins and Shepherd (2010) which is based on 8 years of data

773 (1998-2005) collected by 16 SuperDARN coherent scatter radars. The climatology represented by the CS10

774 model in Fiori et al's Figure 3a indicates speeds in the few hundreds of ms^{-1}, while the instantaneous values

775 along the Swarm satellite pass (their Figure 3d) show much stronger drift peak values on the resolution level of

776 seconds or shorter. Even after allowing for offsets, their 1-sec resolution corrected cross-track ion drifts achieve

777 horizontal velocities well over 1,000 ms^{-1}, which probably indicates the highly dynamic behaviour in the auroral

778 regions compared with quasi-stable conditions used for empirical models. However, recently Koustov et al.

779 (2019) compared the Swarm cross-track ion drifts with the SuperDARN radar network and found that the

780 Swarm ion velocities are a factor of 1.5 larger. They suggest reasons for the disparity, including refining the

781 calibration of Swarm and the differences in spatial/temporal resolution.

782 Aruliah et al. (1996) presented the seasonal and solar cycle variation of hourly averaged ion velocities from 300

783 days of EISCAT Tromsø UHF radar measurements between 1984-1990. The tristatic EISCAT radar

784 observations for an altitude of 275 km were collected from Common Programmes 1, 2 and 3, at time resolutions

785 of 2-3 mins, with full 24 hours coverage. The hourly averaged ion velocities for December solstice periods were

786 up to 100-200 ms^{-1}, and the largest average ion velocities were around 300 ms^{-1} during the March equinox

787 period at solar maximum. Aruliah et al. (2005) later reported observations of a common volume using a

788 configuration of tristatic FPI observations of the thermospheric winds and temperatures co-located with tristatic

789 EISCAT radar measurements of ionospheric parameters at 250 km altitude. The observations showed that the

790 neutral winds were on average around 50% of the magnitude of the ion velocities when averaged over 15 min.

791 Griffin et al. (2004) determined seasonal and solar cycle climatologies of meridional winds at Kiruna using FPI

792 Doppler shifts, and derived from field-aligned ion velocities (Salah and Holt, 1974), which were compared with

793 physical (CTIM, Fuller-Rowell et al., 1988) and empirical models (HWM, Hedin et al, 1988; MWM, Miller et

794 al., 1997). The climatologies all showed meridional winds up to ~250 ms^{-1}. Although this method does not give

795 the zonal wind magnitude, it gives some indication of typical magnitudes owing to the diurnal variation of
796 winds seen by a single site as the Earth rotates.

797 Förster et al. (2008) presented a statistical comparison of observed averaged neutral wind velocities within the
798 polar cap (magnetic latitudes > 80°) for the year 2003 showing the dependence on the IMF orientation based on
799 statistical analyses of CHAMP accelerometer data with average ion drift estimates for the same time interval
800 and IMF conditions based on EDI Cluster measurements. These comparisons were done for both the Northern
801 and the Southern Hemisphere separately in their Tables 1 and 2, respectively. Depending on the IMF clock
802 angle orientation, the ratio between average neutral wind magnitudes and average ion drift speeds varies
803 between about 60% and around 100%. Interestingly, there is a characteristic interhemispheric difference with
804 respect to the IMF orientation and slightly larger ion drift velocities on average in the Northern Hemisphere (cf.
805 Förster and Cnossen, 2013; Förster et al., 2017), but the overall average amounts to a ratio of about 0.90 to 0.95
806 for, note well, within the polar cap region > 80° magnetic only. The FPI in Longyearbyen at 75.4° N (see Table
807 2) comes closest to this region. Ion drag is the dominating forcing term here for the neutral gas, while near the
808 auroral oval, where the KEOPS FPI station in Kiruna at 65.1° N is located, the balance between the different
809 forces, in particular pressure gradient terms, Coriolis and centrifugal forces, and ion drag, play a role. There the
810 ratio between the average neutral wind and ion drag magnitudes is certainly smaller, corresponding to the
811 EISCAT observations cited above.

812

813 **7 Conclusions**

814

815 A comparison is presented here of thermospheric zonal winds during winter months between 2001-2007
816 measured by the CHAMP satellite in the altitude region 350-400 km, and by ground-based FPIs, at Kiruna and
817 Longyearbyen, measured at about 240 km altitude. The satellite accelerometer measurements of drag are used to
818 derive cross-track winds, while the FPIs use the Doppler shift of the 630 nm emission. The satellite
819 measurements are collected for a region within 2° latitude of the FPI sites, which is within the field of view of
820 the FPI East and West look directions. The phases of the winds agree very well, but the CHAMP average zonal
821 winds are a factor 1.5-2.0 larger than the FPI average zonal winds. The factor is not simple. In particular there is
822 a difference in the factor for the auroral site and the polar cap site, so it appears that the factor is dependent on
823 location, possibly latitude. The factor also appears to have an irregular time dependence.

824 The UCL Longyearbyen FPI winds are consistent with FPI measurements made 20 years previously by the
825 University of Alaska using a different FPI and detector (photometer in 1980, EMCCD in 2001). Earlier studies
826 of average ion velocities from the EISCAT Tromsø UHF radar compared with the UCL FPI at KEOPS indicate
827 that in the auroral zone the average ion velocities are about twice the average neutral wind speeds (Aruliah et al.,
828 1996 and 2005). However, the CHAMP average zonal winds at KEOPS presented here have magnitudes similar
829 to the average _ion_ velocities of the December solstice values presented by Aruliah et al (1996). This is probably
830 the key argument indicating that the CHAMP magnitudes are too large. It is important to determine the absolute
831 wind values correctly since the difference between the ion and neutral winds determine the amount of Joule
832 heating of the thermosphere.

Satellites play a crucial role in upper atmosphere research by filling in the extensive gaps between ground-based observations. Satellites provide 3-dimensional coverage at high spatial resolution, in addition to high temporal resolution. Meanwhile, ground-based instruments are sparse, land-based, and not always operational on a 24/7 basis owing to operational costs (e.g. incoherent scatter radars) or observing constraints (e.g. only night-time and clear sky observations for optical instruments). Having uncovered this discrepancy between ground-based FPI optical measurements and satellite drag measurements of winter winds, it is imperative to determine if it is a real altitude dependence, or if some re-scaling of winds, is necessary for winds determined from either, or both, of FPI height-integrated Doppler shifts or satellite drag measurements. Both possibilities will affect our current modelling of the upper atmosphere. We may also need to rethink the procedure of comparing different spatial and temporal resolutions of in-situ satellite versus remote ground-based FPI measurements in terms of the geometry of cross-track winds at high latitudes.

Author contributions. This paper is the result of many years of collaboration between AA and MF after noticing the significant difference between FPI and CHAMP winds. AA provided the FPI data, MF provided the CHAMP data. RH provided the model simulations, IM provided technical support for the FPIs, and ED provided expertise on converting accelerometer data to winds.

Competing interests. The authors declare that they have no conflict of interest.

Data availability. The CHAMP accelerometer neutral wind observations used in this study are available at http://doi.org/10.5880/GFZ.1.1.2019.001 (Förster and Doornbos, 2019).

Acknowledgements. We thank the staff at the Kjell Henriksen Observatory and ESRANGE for hosting the FPIs and their generous on-site assistance. Support for the FPI operations have come from the European Office of Aerospace Research and Development (grant FA9550-17-1-0019). There has been NERC support of ALA (grants NE/P001556/1 and NE/N004051/1). The CHAMP mission is sponsored by the Space Agency of the German Aerospace Center (DLR) through funds of the Federal Ministry of Economics and Technology, following a decision of the German Federal Parliament (grant code 50EE0944). The data retrieval and operation of the CHAMP satellite by the German Space Operations Center (GSOC) of DLR is acknowledged. EISCAT is an international association supported by research organisations in China (CRIRP), Finland (SA), France (CNRS, till end 2006), Germany (DFG), Japan (NIPR and STEL), Norway (NFR), Sweden (VR), and the United Kingdom (STFC). We also acknowledge support from the International Space Science Institute for sponsoring meetings of the international team #308 on 'M-I-T Coupling: Differences and similarities between the two hemispheres', which helped this collaboration (http://www.issibern.ch/teams/twohemispheres/).

870   **References:**

871   Anderson, C., Conde, M., and McHarg, M. G.: Neutral thermospheric dynamics observed with two scanning
872   Doppler imagers: 1. Monostatic and bistatic winds, J. Geophys. Res.,117, A03304,
873   doi:10.1029/2011JA017041, 2012.

874   Aruliah A.L., Rees, D.: The Trouble with Thermospheric Vertical Winds: Geomagnetic, Seasonal and Solar
875   Cycle Dependence at High Latitudes, J. Atmos. Terr. Phys., 57, 597-609, 1995

876   Aruliah A.L., Farmer, A. D., Rees, D., Brändström, U.: The Seasonal Behaviour of High-Latitude
877   Thermospheric Winds and Ion Velocities Observed Over One Solar Cycle, J. Geophys. Res., 101, 15701-
878   15711, 1996

879   Aruliah, A. L. and Griffin, E. M.: Evidence of meso-scale structure in the high-latitude thermosphere, Ann.
880   Geophys., 37–46, 2001.

881   Aruliah, A. L., Griffin, E. M., Aylward, A. D., Ford, E. A. K., Kosch, M. J., Davis, C. J., Howells, V. S. C.,
882   Pryce, E., Middleton, H., Jussila, J.: First direct evidence of meso-scale variability on ion-neutral dynamics
883   using co-located tristatic FPIs and EISCAT radar in Northern Scandinavia, EISCAT workshop special issue
884   Annales Geophys., 23, 147-162, 2005

885   Bauer, S.J.: Physics and chemistry in space, Vol 6 of Physics of planetary ionospheres, Springer-Verlag, 1973

886   Bruinsma, S. L., Doornbos, E., Bowman, B.R.: Validation of GOCE densities and evaluation of thermosphere
887   models Advances in Space Research, Volume 54, Issue 4, 576-585.10.1016/j.asr.2014.04.008, 2014.

888   Cook, G.E.: Satellite drag coefficients, Planet. Space Sci., 13, 929, 1965

889   Cousins, E. D. P., and S. G. Shepherd (2010), A dynamical model of high‐latitude convection derived from
890   SuperDARN plasma drift measurements, J. Geophys. Res., 115, A12329, doi:10.1029/2010JA016017.

891   Dalgarno, A., and Smith, F. J.: The thermal conductivity and viscosity of atomic oxygen, Planet.Space.Sci., 9, 1-
892   2, 1962.

893   Davies, J.A., Lester, M., Milan, S.E., Yeoman, T. K.: A comparison of velocity measurements from the
894   CUTLASS Finland radar and the EISCAT UHF system, Ann.Geophys., 17, 892-902, 1999.

895   Deehr, C. S., Sivjee, G. G., Egeland, A., Henriksen, K., Sandholt, P. E., Smith, R., Sweeney, P., Duncan, C.,
896   Gilmer, J.: Ground-based observations of F region aurora associated with the magnetospheric cusp, J.
897   GEOPHYS. RES., 85, 2185-2192, 10.1029/JA085iA05p02185, 1980.

898   Dhadly, M., Emmert, J., Drob, D., Conde, M., Doornbos, E., Shepherd, G., Makela, J., Wu, Q., Niciejewski, R.,
899   and Ridley, A.: Seasonal dependence of northern high-latitude upper thermospheric winds: A quiet time
900   climatological study based on ground-based and space-based measurements, Journal of Geophysical
901   Research (Space Physics), 122, 2619-2644, 10.1002/2016JA023688, 2017

902   Dhadly, M., Emmert, J., Drob, D., Conde, M., Shepherd, G., Makela, J., Wu, Q., Niciejewski, R., and Ridley,
903   A.: Seasonal Dependence of geomagnetic active-time northern high-latitude upper thermospheric winds, J.
904   GEOPHYS. RES., 123, 739-754, https://doi.org/10.1002/2017JA024715, 2018

905   Doornbos, E, Ijssel, J., Lühr, H., Förster, M., and Koppenwallner, G:. Neutral density and crosswind
906   determination from arbitrarily oriented multiaxis accelerometers on satellites. Journal of Spacecraft and
907   Rockets, 47(4): 580–589, 2010. doi:10.2514/1.48114, 2010

908   Drob, D. P., Emmert, J. T., Meriwether, J. W., Makela, J. J., Doornbos, E, Conde, M., Hernandez, G., Noto, J.,
909   Zawdie, K. A., McDonald, S. E., Huba, J. D., and Klenzing, J. H.: An update to the Horizontal Wind Model

(HWM): The quiet time thermosphere, Earth and Space Science, 2, 301-319, 10.1002/2014EA000089, https://doi.org/10.1002/2014EA000089,2015

Emmert, J.T., Hernandez, G., Jarvis, M. J., Niciejewski, R. J., Sipler, D. P., and Vennerstrom, S.: Climatologies of nighttime upper thermospheric winds measured by ground-based Fabry-Perot interferometers during geomagnetically quiet conditions: 2. High-latitude circulation and interplanetary magnetic field dependence, J. Geophys. Res., 111, A12303, doi:10.1029/2006JA011949, 2006b.

Fiori, R. A. D., Koustov, A. V., Boteler, D. H., Knudsen, D. J., & Burchill, J. K.: Calibration and assessment of Swarm ion drift measurements using a comparison with a statistical convection model. Earth, Planets and Space, 68(1), 100. http://doi.org/10.1186/s40623-016-0472-7, 2016.

Forbes, J. M., Roble, R. G., and Marcos, F. A.: Magnetic activity dependence of high–latitude thermospheric winds and densities below 200 km, J. Geophys. Res., 98, 13,693–13,702, 1993.

Ford, E.A.K., Aruliah, A.L., Griffin, E.M., McWhirter, I.: High time resolution measurements of the thermosphere from Fabry-Perot Interferometer measurements of atomic oxygen, Annales Geophys., 25, 1269 – 1278, 2007.

Förster, M., Rentz, S., Köhler, W., Liu, H., and Haaland, S. E.: IMF dependence of high-latitude thermospheric wind pattern derived from CHAMP cross-track measurements, Ann. Geophys., 26, 1581–1595, 2008.

Förster, M., Haaland, S.E., and Doornbos, E., Thermospheric vorticity at high geomagnetic latitudes from CHAMP data and its IMF dependence, Ann. Geophys., 29, 181-186, doi:10.5194/angeo-29-181-2011, 2011.

Förster, M., and Cnossen, I.: Upper atmosphere differences between northern and southern high latitudes: The role of magnetic field asymmetry, J. Geophys. Res. Space Physics, *118*, 5951–5966, doi:10.1002/J.Geophys.Res.a.50554, 2013.

Förster, M., Doornbos, E., and Haaland S.: The role of the upper atmosphere for dawn-dusk differences in the coupled magnetosphere-ionosphere-thermosphere system", in: Dawn-Dusk Asymmetries in Planetary Plasma Environments, eds. Stein Haaland, Andrei Runov and Colin Forsyth, John Wiley Publications, AGU Geophysical Monograph, Vol. 230, 125-142, ISBN: 978-1-119-21632-2, 2017.

Förster, Matthias; Doornbos, Eelco (2019): Upper thermosphere neutral wind cross-track component deduced from CHAMP accelerometer data. GFZ German Research Centre for Geosciences. http://doi.org/10.5880/GFZ.1.1.2019.001

Foster, J. C., Holt, J. M., Musgrove, R. G., and Evans, D. S.: Ionospheric convection associated with discrete levels of particle precipitation, Geophys. Res. Lett., 13, 656, 1986.

Fuller-Rowell, T. J.: Modelling the solar cycle change in nitric oxide in the thermosphere and upper mesosphere, J. Geophys. Res., 98, 1571, 1992.

Fuller-Rowell, T.J., Rees, D.: Interpretation of an Anticipated Long-Lived Vortex in the Lower Thermosphere Following Simulation of an Isolated Substorm, Planet. Space Sci., 32, 69-85, 1984

Fuller-Rowell T.J., Evans, D.S.: Height Integrated Pedersen and Hall Conductivity Patterns Inferred from the TIROS-NOAA Satellite Data, J. GEOPHYS. RES., 92, 7606-7618, 1987

Fuller-Rowell, T. J., Rees, D., Quegan, S., Moffett, R. J., Bailey, G.J.: Simulations of the seasonal and UT variations of the thermosphere and ionosphere using a coupled, three-dimensional, global model, Pur. A. Geoph., 127, 189–217, 1988.

949 Fuller-Rowell, T. J., Rees, D., Quegan, S., Moffett, R. J., Codrescu, M. V., and Millward, G. H.: A coupled
950   thermosphere ionosphere model, Solar terrestrial energy program (STEP), handbook of ionospheric models,
951   (Ed) Schunk, R. W., 1996.

952 Gillies, M. D., Knudsen, D., Donovan, E., Jackel, B., Gillies, R., Spanswick, E.: Identifying the 630 nm auroral
953   arc emission height: A comparison of the triangulation, FAC profile, and electron density methods, J.
954   Geophys. Res. Space Physics, 122, doi:10.1002/2016JA023758, 2017.

955 Griffin, E.M., Aruliah, A. L., Müller-Wodarg, I. C. F., Aylward, A. D.: Comparison of High-Latitude
956   Thermospheric Meridional Winds II: Combined FPI, Radar and Model Climatologies, Ann. Geophys, 22,
957   863-876, 2004.

958 Griffin, E. M., Müller-Wodarg, I. C. F., Aruliah, A., and Aylward, A.: Upper thermospheric neutral wind and
959   temperature measurements from an extended spatial field, Ann. Geophys., 26, 2649– 2655, 2008.

960 Harang, L.: The mean field of disturbance of polar geomagnetic storms, Terr. Mag. Atmos. Elec., 51, 353-380,
961   1946.

962 Harris, M.: A New Coupled Middle Atmosphere and Thermosphere General Circulation Model: Studies of
963   Dynamic, Energetic and Photochemical Coupling in the Middle and Upper Atmosphere. PhD Thesis,
964   University of London, 2001

965 Harris, M. J., Arnold, N. F., and Aylward, A. D.: A study into the effect of the diurnal tide on the structure of
966   the background mesosphere and thermosphere using the new coupled middle atmosphere and thermosphere
967   (CMAT) general circulation model, Ann. Geophys., 20, 225–235, doi:10.5194/angeo-20-225-2002, 2002.

968 Hecht, E., Zajac, A.: Optics, Addison-Wesley Publishing Company, 1980.

969 Hedin A. E., Salah, J. E., Evans, J. V., Reber, C. A., Newton, G. P., Spencer, N. W., Kayser, D. C., Alcayde, D.,
970   Bauer, P., Cogger, L., McClure, J. P.: A Global Thermospheric Model Based on Mass Spectrometer and
971   Incoherent Scatter Data MSIS 1. N_2 Density and Temperature, J.Geophys.Res., 82, 2139-2147, 1977.

972 Hedin A.E., Biondi, M. A., Burnside, R. G., Hernandez, G., Johnson, R. M., Killeen, T. L., Mazaudier, C.,
973   Meriwether, J. W., Salah, J. E., Sica, R. J., Smith, R. W., Spencer, N. W., Wickwar, V. B., Virdi, T. S.:
974   Revised Global Model of Thermospheric Winds Using Satellite and Ground-Based Observations, J.
975   Geophys. Res. Space Physics, 96, 7657-7688, 1991.

976 Hedin, A. E., et al. (1996), Empirical wind model for the upper, middle and lower atmosphere, J. Atmos. Terr.
977   Phys., 58, 1421–1447, doi:10.1016/0021-9169(95)00122-0.

978 Helleputte, T. V., Doornbos, E., and Visser, P.: CHAMP and GRACE accelerometer calibration by GPS-based
979   orbit   determination.   Advances   in   Space   Research,   43(12),   1890–1896.
980   http://doi.org/10.1016/j.asr.2009.02.017, 2009.

981 Hood, R. K. E., Effects of field-aligned currents in the ionosphere-thermosphere system, PhD Thesis, University
982   College London, UK, 2018

983 Jacchia, L. G., and Slowey, J. W.: A supplemental catalog of atmospheric densities from satellite-drag analysis
984   (No. 348). SAO Special Report, 1972.

985 Killeen, T. L., Smith, R. W., Hays, P. B., Spencer, N. W., Wharton, L. E., McCormac, F. G.: Neutral winds in
986   the high latitude winter F-region: Coordinated observations from ground and space, Geophys. Res. Lett., 11,
987   311-314, 1984.

988 Killeen T.L., Won, Y.-I., Niciejewski, R.J., Burns, A.G.: Upper Thermosphere Winds and Temperatures in the
989   Geomagnetic Polar Cap: Solar Cycle, Geomagnetic Activity and IMF Dependencies, J. Geophys. Res., 100,
990   21327-21342, 1995.

991 Koustov, A. V., Lavoie, D. B., Kouznetsov, A. F., Burchill, J. K.,Knudsen, D. J., & Fiori, R. A. D., A
992   comparison of cross-track ion drift measured by the Swarm satellites and plasma convection velocity
993   measured by SuperDARN. Journal of Geophysical Research: Space Physics, 124, 4710-4724.
994   https://doi.org/10.1029/2018JA026245, 2019.

995 Liu, H., Lühr, H., Henize, V., and Köhler, W.: Global distribution of the thermospheric total mass density
996   derived from CHAMP, J. Geophys. Res., 110, A04301, doi:10.1029/2004JA010741, 2005.

997 Liu, H., Lühr, H.,Watanabe, S., Köhler,W., Henize, V., and Visser, P.: Zonal winds in the equatorial upper
998   thermosphere: Decomposing the solar flux, geomagnetic activity, and seasonal dependencies, J. Geophys.
999   Res., 111, A07307, doi:10.1029/2005JA011415, 2006.

1000 Liu, H., Doornbos, E., & Nakashima, J.: Thermospheric wind observed by GOCE: Wind jets and seasonal
1001   variations. Journal of Geophysical Research: Space Physics, 121(7), 6901–6913.
1002   http://doi.org/10.1002/2016JA022938, 2016.

1003 Liu, X., Xu, J., Yue, J. & Vadas, S. L., Numerical modeling study of the momentum deposition of small
1004   amplitude gravity waves in the thermosphere, Annales Geophysicae, 31(1), 1-14, 2013

1005 Makela, J. J., Meriwether, J. W., Huang, Y., Sherwood, P. J.: Simulation and analysis of a multi-order imaging
1006   Fabry-Perot interferometer for the study of thermospheric winds and temperatures, Applied Optics, 50,
1007   4403-4416, 2011.

1008 March, G., Doornbos, E. N. and Visser, P. N. A. M.: High-fidelity geometry models for improving the
1009   consistency of CHAMP, GRACE, GOCE and Swarm thermospheric density data sets, Advances in Space
1010   Research, 63, 213-238, 10.1016/j.asr.2018.07.009, 2018.

1011 March, G., E. N. Doornbos, and P. N. A. M. Visser, High-fidelity geometry models for improving the
1012   consistency of CHAMP, GRACE, GOCE and Swarm thermospheric density data sets, Advances in Space
1013   Research, 63, 213-238, 10.1016/j.asr.2018.07.009, 2019

1014 Marcos, F. A. and Forbes, J. M.: Thermospheric wind from the satellite electrostatic triaxial accelerometer
1015   system, J. Geophys. Res., 90, 6543–6552, 1985.

1016 McWhirter I., Rees, D., Greenaway, A. H.: Miniature Imaging Photon Detectors III.~An Assessment of the
1017   Performance of the Resistive Anode IPD, J. Phys. E.: Sci. Instrum., 15, 145-150, 1982.

1018 McWhirter, I., Electron Multiplying CCDs - New Technology for Low Light Level Imaging, Proceedings of
1019   33rd Annual European Meeting on Atmospheric Studies by Optical Methods, IRF Sci. Rep., 292, 61-66,
1020   2008.

1021 Mehta, P. M., Walker, A. C., Sutton, E., & Godinez, H. C.: New density estimates derived using accelerometers
1022   on-board the CHAMP and GRACE satellites. Space Weather, 15(4), 558–576.
1023   http://doi.org/10.1002/2016SW001562, 2017.

1024 Moe, Mildred. M., Wallace, Steven D., Moe, Kenneth : The upper mesosphere and lower thermosphere, A
1025   review of experiment and theory, Geophysical Monograph 87, 1995

1026 Quegan, S., Bailey, G. J., Moffett, R. J., Heelis, R. A., Fuller-Rowell, T. J., Rees, D., and Spiro, A. W.: A
1027   theoretical study of the distribution of ionisation in the high-latitude ionosphere and the plasmasphere: First
1028   results of the mid-latitude trough and the light ion trough, J. Atm. Terr. Phys., 44, 619, 1982.

1029 Rees, D., Fuller-Rowell, T. J., Gordon, R., Smith, M. F., Maynard, N. C., Heppner, J. P., Spencer, N. W.,
1030   Wharton, L., Hays, P. B., and Killeen, T. L.: A theoretical and empirical study of the response of the high
1031   latitude thermosphere to the sense of the "Y" component of the interplanetary magnetic field, Planet. Space
1032   Sci., 34, 1–40, 1986.

1033 Reigber, C., Lühr, H., and Schwintzer, P.: CHAMP mission status, Adv. Space Res., 30, 129–134, 2002.

1034 Roble, R. G., Ridley E. C., and Dickenson, R. E.: On the global mean structure of the thermosphere, J. Geophys.
1035   Res., 92, A8, 8745–8758, 1987.

1036 Ronksley, Amy, Optical remote sensing of mesoscale thermospheric dynamics above Svalbard and Kiruna, PhD
1037   thesis, UCL, London, UK., 2016.

1038 Salah, J. E. and Holt, J. M.: Midlatitude thermospheric winds from incoherent scatter radar and theory, Radio
1039   Sci., 9, 301–313, 1974.

1040 Schlegel, K., Lühr, H., St.-Maurice, J.-P., Crowley, G., and Hackert, C.: Thermospheric density structures over
1041   the polar regions observed with CHAMP, Annales Geophysicae, 23, 1659–1672, 2005.

1042 Shepherd, S. G.: Altitude-adjusted corrected geomagnetic coordinates: Definition and functional
1043   approximations, J. Geophys. Res. Space Physics, 119, doi:10.1002/2014JA020264, 2014.

1044 Sica R. J., Rees, M. H., Roble, R. G., Hernandez, G., Romick, G. J.: The Altitude Region Sampled by Ground-
1045   Based Doppler Temperature Measurements of the OI 15867K Emission Line in Aurorae, Planet. Space Sci.,
1046   34, 483-488, 1986.

1047 Song, P., Vasyliūnas, V. M., and Zhou, X.-Z.: Magnetosphere-ionosphere/thermosphere coupling: Self-
1048   consistent solutions for a one-dimensional stratified ionosphere in three-fluid theory, J. Geophys. Res., 114,
1049   A08213, doi:10.1029/2008JA013629, 2009.

1050 Song, P., and Vasyliūnas, V. M.: "Inductive-dynamic coupling of the ionosphere with the thermosphere and the
1051   magnetosphere", in: 'Modeling the Ionosphere-Thermosphere System', edited by J. Huba, R. Schunk, and G.
1052   Khazanov, American Geophysical Union, Washington DC,10.1029/2012GM001308, Geophysical
1053   Monograph Series 201, 201-215, 2013.

1054 Sutton, E. K., Nerem, R. S., & Forbes, J. M.: Density and Winds in the Thermosphere Deduced from
1055   Accelerometer Data. Journal of Spacecraft and Rockets, 44(6), 1210–1219. http://doi.org/10.2514/1.28641,
1056   2007.

1057 Tapley, B.D., Bettadpur, S., Watkins, M., and Reigber, C.: The gravity recovery and climate experiment:
1058   Mission overview and early results, Geophys. Res. Lett., 31, L09607, DOI: 10.1029/2004GL019920, 2004.

1059 Torr, M. R., Richards, P. G., and Torr, D. G.: A new determination of ultraviolet heating efficiency in the
1060   thermosphere, J. Geophys.Res., 85, 6819, 1980a.

1061 Torr, M. R., Richards, P. G., and Torr, D. G.: The solar ultraviolet heating efficiency in the mid-latitude
1062   thermosphere, Geophys.Res. Lett., 6, 673, 1980b.

1063 Vadas, S. L. and Crowley, G.: Neutral wind and density perturbations in the thermosphere created by gravity
1064   waves observed by the TIDDBIT sounder, J. Geophys. Res. Space Physics, *122*, 6652–6678,
1065   doi:10.1002/2016JA023828, 2017.

1066 Visser, T., March, G., Doornbos, E., de Visser, C., & Visser, P.: Horizontal and vertical thermospheric cross-
1067   wind from GOCE linear and angular accelerations. Advances in Space Research.
1068   http://doi.org/10.1016/j.asr.2019.01.030, 2019.

1069 Vlasov, M. N., Nicolls, M. J., Kelley, M. C., Smith, S. M., Aponte, N., and Gonzalez, S. A: Modeling of
1070   airglow and ionospheric parameters at Arecibo during quiet and disturbed periods in October 2002, J.
1071   Geophys. Res., 110, A07303, doi:10.1029/2005JA011074, 2005.

1072 Yiu, H.C.I: High latitude thermosphere meso-scale studies and long-term database investigations with the new
1073   Scanning Doppler Imager and Fabry-Perot Interferometers, Ph.D. Thesis, Univ. of London, London, UK,
1074   2014.